INFORMATION TO USERS

This manuscript has been reproduced from the microfilm master. UMI films the text directly from the original or copy submitted. Thus, some thesis and dissertation copies are in typewriter face, while others may be from any type of computer printer.

The quality of this reproduction is dependent upon the quality of the copy submitted. Broken or indistinct print, colored or poor quality illustrations and photographs, print bleedthrough, substandard margins, and improper alignment can adversely affect reproduction.

In the unlikely event that the author did not send UMI a complete manuscript and there are missing pages, these will be noted. Also, if unauthorized copyright material had to be removed, a note will indicate the deletion.

Oversize materials (e.g., maps, drawings, charts) are reproduced by sectioning the original, beginning at the upper left-hand corner and continuing from left to right in equal sections with small overlaps.

Photographs included in the original manuscript have been reproduced xerographically in this copy. Higher quality 6" x 9" black and white photographic prints are available for any photographs or illustrations appearing in this copy for an additional charge. Contact UMI directly to order.

ProQuest Information and Learning
300 North Zeeb Road, Ann Arbor, MI 48106-1346 USA
800-521-0600

UMI®

Reproduced with permission of the copyright owner. Further reproduction prohibited without permission.

DISSERTATION

Investigation of Spatial Variations in Collection Efficiency of Solar Cells

Submitted by
Jason F. Hiltner
Department of Physics

In partial fulfillment of the requirements

for the Degree of Doctor of Philosophy

Colorado State University

Fort Collins, Colorado

Spring 2001

Bell & Howell Information and Learning Company
300 North Zeeb Road
P.O. Box 1346
Ann Arbor, MI 48106-1346

Colorado State University

January 23, 2001

WE HEREBY RECOMMEND THAT THE DISSERTATION PREPARED UNDER OUR SUPERVISION BY JASON F. HILTNER ENTITLED INVESTIGATION OF SPATIAL VARIATIONS IN COLLECTION EFFICIENCY OF SOLAR CELLS BE ACCEPTED AS FULFILLING IN PART REQUIREMENTS FOR THE DEGREE OF DOCTOR OF PHILOSOPHY.

Graduate Committee

Mart P. Gelfand

Stuart Field

James R. Sites
Advisor

David A. Krueger
Department Head

ABSTRACT

INVESTIGATION OF SPATIAL VARIATIONS IN COLLECTION EFFICIENCY OF SOLAR CELLS

In an effort to investigate spatial variations in solar cells, an apparatus which is capable of mapping collection efficiency with micron resolution and near-solar intensity has been developed. Local reductions in collection are observed in CdTe- and $Cu(In_{1-x}Ga_x)Se_2$-based devices, and are characterized by measuring the response as a function of cell bias and incident laser intensity. By modeling this data with an equivalent circuit, it is clear that the majority of local variations in the response are due to series resistance variations. Further, direct evidence is given for bandgap variations in CdTe solar cells, which are correlated with high resistance regions in some devices. The bandgap variation is attributed to diffusion of S into CdTe, forming the lower bandgap $CdTe_{1-x}S_x$, during the post-deposition $CdCl_2$ treatment commonly used to improve performance. Investigation of the impact of $CdCl_2$ on a CdTe solar cell indicates that the treatment reduces the number of variations seen with above-bandgap photon energies, but also increases local variations in bandgap. The latter effect has been attributed to non-uniform penetration of $CdCl_2$ to the device interface. Finally, elevated-temperature stress on CdTe devices is shown to preferentially degrade regions which exhibit decreases in bandgap, and hence increased S alloying.

Jason F. Hiltner
Physics Department
Colorado State University
Fort Collins, CO 80523
Spring 2001

ACKNOWLEDGMENTS

This work has been aided in no small measure by my advisor Jim Sites, who has shown a great willingness to let his students present material and interact directly with other scientists in the field. This experience has been invaluable, as has the opportunity to work with him. Thanks for all the help along the way, and especially for your patient help with this thesis.

Thanks also to my committee members Marty Gelfand, Carmen Menoni, and Stuart Field for reviewing this work. Thanks to Stuart for stepping in at the last minute and for the experimental help. The optics advice from Siu Au Lee, and design help from Dave Warner and also Jay Jablonski made this possible, thank you. Cheers and good luck to my colleagues at CSU: Jennifer Granata, Pam Johnson, Markus Gloeckler, and Alexie Pudov, thanks for all of your help.

Several scientists have provided their time and expertise in preparing key samples specifically for this work. They include David Albin at NREL, Brian McCandless at IEC, and Doug Rose at First Solar. Thank you for taking the time to get me such great sets of cells, and for the many valuable discussions. Thanks also to the CSU Materials Research Group, Jeff Britt at Global Solar, and Xuanzhi Wu, Miguel Contreras, and Sarah Kurtz at NREL for providing samples. Thanks also to the members of the National CdTe and CIGS teams.

I will miss a great many people in Fort Collins who have lived well with me over the years. Here's to Peterson Street – I hope I live again in a neighborhood filled with half so many great people. Dave and Ann Marie, Brian and Ilsa, thanks for being such great friends.

To Shannon I owe so much. You alone know what too much work can do to me. Thank you for not letting me grow too fractious, for supporting my zeal, and for bringing me through the stress of completing.

Table of Contents

List of Figures

List of Tables

Chapter 1

Introduction

Solar cells hold the promise of clean renewable energy. The impact they will eventually hold on the global energy market is likely to be extremely significant, given recent advances in making the technology less expensive to produce and deploy. The supply of fossil fuels will inevitably dwindle, leading to a worldwide demand for a new source of power. Due to global warming, ozone depletion, and other environmental concerns, the replacement technology will likely be one such as solar photovoltaic power, which produces very little pollution during its fabrication, none while in use, and also very little at the end of its lifecycle if recyling programs are implemented [1].

Solar cells based on thin-film polycrystalline materials may provide much of the answer to inexpensive, widely available solar energy. With high speed, large area deposition of semiconductor materials on glass or other substrates, some sacrifice in efficiency compared to single-crystal technologies will likely be made. However, efficiencies up to 18.8% have been demonstrated, and the lower cost of materials promises lower end prices for the consumer. The ability to coat large areas is a very important point, since prices will go down as the scale of production goes up.

Several challenges present themselves when developing polycrystalline materials for large scale terrestrial applications. While research cells have achieved efficiencies comparable to single crystalline material [2], issues such as local defects and overall uniformity become increasingly important as the deposition area is increased. In addition, performing research on polycrystalline materials is not always straightforward because of the interactions between different layers of the solar cell. These interactions make it more difficult to determine the effects of a change in processing; for example, changing the temperature of CdTe deposition will not only affect the CdTe growth, but will also affect previously deposited layers.

Polycrystalline materials, however, can be remarkably forgiving, and do have several advantages over crystalline materials. Reasonable efficiencies can be produced by many different processing methods, with speeds of fabrication ranging from $10\ \mu\mathrm{m} / \mathrm{min}$ to $1\ \mu\mathrm{m} / \mathrm{h}$. Modules may be fabricated monolithically, also decreasing processing costs. Finally, novel substrates such as polyamide may be used in the near future, which would reduce costs due to ease of processing and reductions in shipping costs.

The goals of this thesis follow from the fact that electrical measurements are usually performed on finished devices, and characterize the entire area of the cell as a whole. Non-uniformity effects which cause losses in device performance cannot be separated from overall losses (such as losses due to a uniformly high series resistivity). The polycrystalline nature of the cells suggest that local defects such as local shunts and recombination centers may be present. The strong dependence on fabrication parameters also suggests that gradations of material quality may be present in different parts of the cell. For example, the growth of material often depends strongly on the substrate temperature, which may contain variations due to the geometry of the fabrication setup. A method for exploring the effects of non-uniformites and defects thus may help explain lower efficiencies in solar cell devices. The apparatus constructed, the measurements presented, and the analysis performed should then all be viewed with the overall goal in mind: understanding the impact of non-uniformity and local defects on device performance, with the idea of improving the conversion efficiency of economically viable solar cells.

Focusing a laser onto the solar cell and measuring the resulting photocurrent can generate a map related to the local response of the solar cell. The collected photocurrent probes local variations in the device, including the local quality of the junction, spatial variation in the resistivity, and local shunting effects. This technique, therefore, should yield information directly applicable to the question of uniformity and the density of local defects.

This technique has also been applied to polycrystalline silicon devices, which have grain sizes typically 100 times greater than those in typical polycrystalline CdTe and CIGS material. In addition to addressing the uniformity of the material, researchers have devised means of extracting parameters related to carrier dynamics, such as the minority carrier diffusion length, with measurements of the response near a grain boundary in the material. It will be shown that, because of the much smaller grain sizes and other concerns specific to thin-film devices, one cannot apply all of these analyses to thin-film solar cells. Instead, the analysis of the results presented in this thesis will include circuit analysis, which is one step removed from carrier dynamics.

The apparatus developed in this thesis provides a unique characterization of the uniformity of collection efficiency at multiple resolutions. At the lowest resolution, the entire area of a research-size device may be mapped. At the highest resolution, the response of single grains can be examined – using a probe which duplicates field conditions, including an intensity similar to standard solar intensity. This is an advantage over other techniques such as EBIC (electron beam induced current) and NSOM (near field scanning optical microscopy), which offer much higher resolution, but do not duplicate the conditions that the solar cell will experience in normal operation.

The most significant problem with this technique is the interpretation of the data, especially in the case of polycrystalline thin films. To a lesser extent, routine application of this technique can be hampered by technical difficulties and the length of time necessary to generate a complete set of data which well characterizes the sample. Recent advances in optical fiber technology have made the diffraction-limited performance in the apparatus attainable, and future related advances will remove a great deal of the remaining technical barriers. Customized computer applications have shortened the time necessary to take the data, and have made the system almost fully automatic. It is hoped that these advances will allow this type of measurement to be applied to the question of uniformity in polycrystalline thin film solar cells.

Chapter 2

Background

A short overview of solar cell devices is given, with emphasis on the issues addressed by this thesis. Electrical characterization and the absorption of light by a semiconductor are introduced, and references are given for more detailed information. Finally, a brief synopsis of previous work on using focused lasers to probe solar cells will be given.

2.1 Thin Film Polycrystalline Solar Cells

The types of devices in this study include CdTe- and $Cu(In_xGa_{1-x})Se_2$-based solar cells. The latter will be referred to as CIGS. These materials are p-type absorbers with bandgaps well matched to the solar spectrum (~1.5 and ~1.15 eV respectively). In both cases, an n-type CdS layer is usually employed as the window layer, though other materials have been used with somewhat poorer best case results. The electronic behavior of these devices can be reasonably well described by standard diode equations with slight modifications. This assumption does break down under certain conditions (such as under high intensity illumination), which will be examined separately.

Figure 2.1 shows the device structures. Note that the CdTe-based cells use glass as a superstrate, so that light must first pass through the glass before it is absorbed by the semiconductor. Detailed information on state-of-the-art CdTe-based solar cells can be found in [3]. A similar reference for CIGS cells can be found in [4].

The materials which comprise the solar cell devices are polycrystalline thin films. CdTe grains are typically 1-5 μm in size, CIGS grains are slightly smaller: 1-2 μm in size.

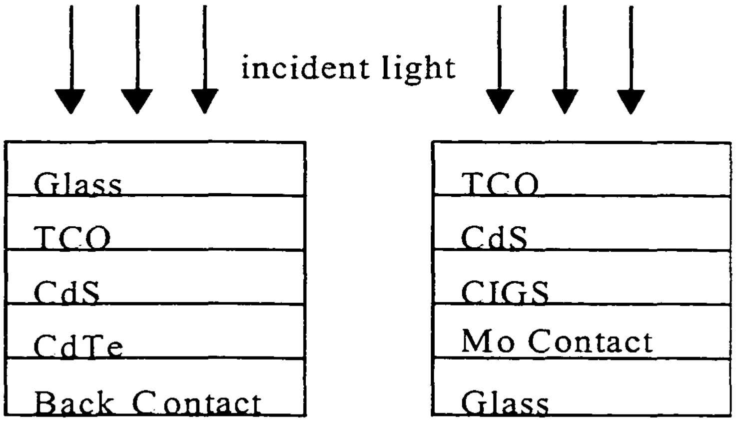

Figure 2.1. Cell device structures (not to scale). TCO stands for transparent conducting oxide.

For these materials to function in electronic devices, it is clear that significant grain boundary passivation must take place. Part of the goal of locally mapping the device response with high resolution is to assess how grain boundaries affect the overall device performance, and how different fabrication techniques and treatments affect the response near a grain boundary. Also, since each layer is polycrystalline, interface regions are expected to be complex in terms of carrier flow and junction formation. This *results in non-uniformity* considerations [5], where the interactions between the grains will lead to local variations in junction potential and resistivity, as well as increased recombination [2]. Therefore a measured photoresponse at each spatial position will need to be subjected to various analytical tools to identify and separate the mechanisms responsible.

2.2 Electrical Characterization

Whole-cell performance evaluation is an essential step in characterizing a solar cell device. From the current-voltage curve one can extract the short-circuit current (J_{sc}), open-circuit voltage (V_{oc}), and fill factor (FF), as well as more detailed information, such as the series resistance and diode quality factor [6]. The whole-cell evaluation of performance is in general a reasonable way of comparing different fabrication processes, particularly since the areas of research-scale devices are the order of 1 cm^2. However, whole-cell measurements are obviously not sensitive to small-scale non-uniformities in junction voltage, current collection, and series resistance. If an entire cell were divided into smaller equal area segments, one would expect some segments to have better performance than others, with the total cell V_{oc} weighted towards the lowest V_{oc} in the set of segments [5], and the total cell J_{sc} given by the mean of the segment J_{sc}'s.

Quantum efficiency (QE) measures the collected photocurrent as a function of wavelength. Each portion of the spectral response is affected by various absorption and collection mechanisms, and so can be interpreted to yield specific insights into the device performance. For example, the effective bandgap of the CdTe layer can be determined from the QE response near 850 nm. Figure 2.2 shows a typical quantum efficiency curve with reflection losses. Shown for reference are the laser wavelengths which were used for the work described in this dissertation. The photon energies were chosen to be slightly below, near, and well above the CdTe bandgap. Each wavelength can be varied downward by about 30 nm by cooling the laser.

2.3 Light Absorption

Incident light is exponentially absorbed within a material, so that the power at a point z (perpendicular to the junction) within the material is given by

$$P(z,\lambda) = P_o(\lambda)\exp\left(-z/\alpha(\lambda)\right) \tag{2.1}$$

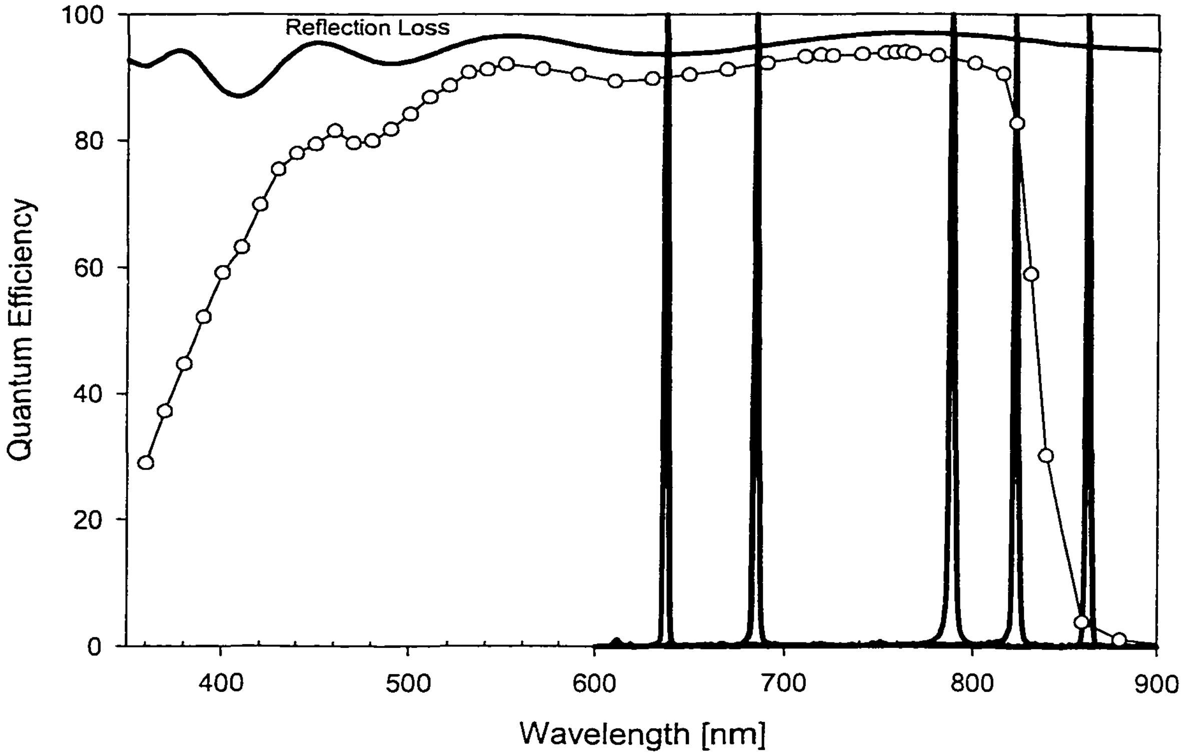

Figure 2.2. Typical quantum efficiency curve for a CdTe cell. Laser wavelengths shown will be discussed in Chapter 3.

where P_o is the power incident at the material boundary, λ is the wavelength and α is the absorption coefficient. Figure 2.3 shows the absorption coefficients for CdTe and CIGS [7–10]. The CIGS curve will shift horizontally if the Ga concentration is varied.

For a direct-band semiconductor, the process of absorption takes place as an electron is excited to the conduction band, leaving a hole in the valence band. In this way minority carriers are injected into the p-type layer, and travel by drift and diffusion processes either through the junction to be collected by the measurement circuit, or are lost due to recombination through various defect processes. Since there are a large number of physical processes that affect absorption and collection issues, the reader is referred to references [11–14] for more detailed information.

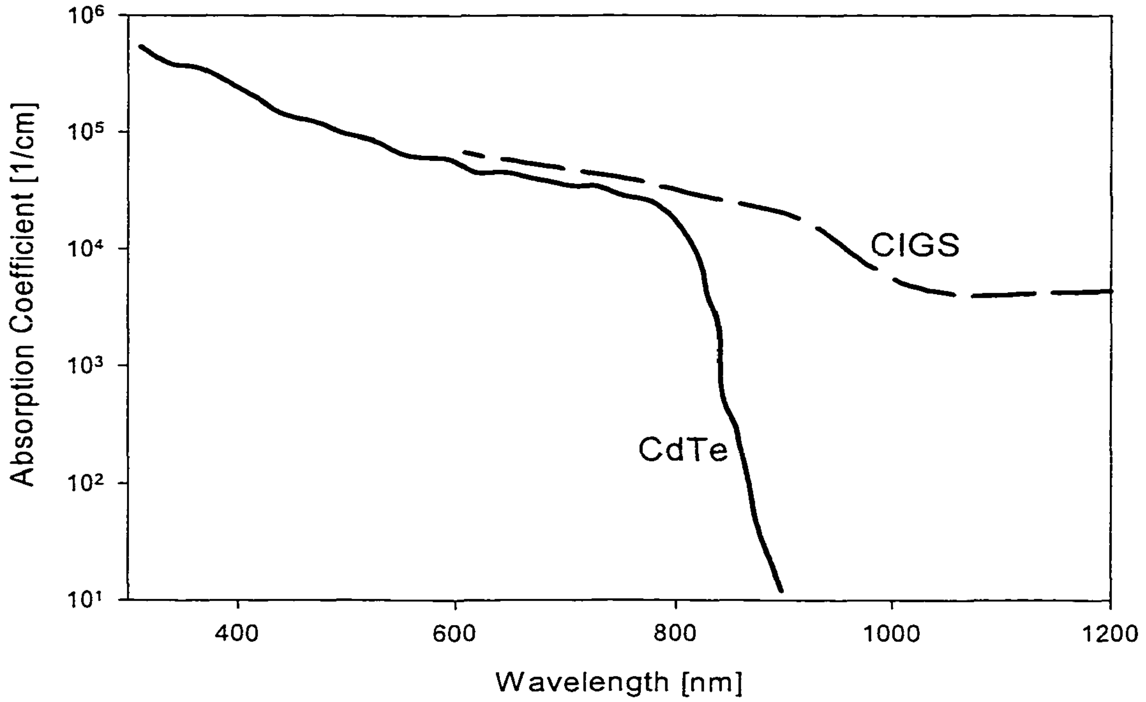

Figure 2.3. Absorption spectra for solar cells used in this study [9, 10].

Typical hole concentrations for p-type CdTe and CIGS in devices are in the 10^{14} and 10^{16} cm^{-3} range, respectively. When the injected electron concentration is the same order as this concentration, a condition referred to as high injection, the usual assumption of neglecting minority carriers breaks down. In addition to the diode behavior changing, the large current implicit in the high injection regime leads to non-negligible voltage drops due to the resistivity of the semiconductors. This subject will be treated in more depth in following chapters.

2.4 Laser Beam Induced Current Measurements

The issue of uniformity is only one example of the type of problem addressed with laser-beam induced current (LBIC) measurements. Various groups have used LBIC to investigate thin-film polycrystalline as-deposited material resistivity [15,16] and post-deposition treatments [17–19]. Polycrystalline silicon has been explored in detail, with much of the work focusing on the response near a grain boundary, including measurement and interpretation of minority carrier diffusion lengths [20–26], where the response near a grain boundary can be evaluated through analytic and numerical means in terms of the minority carrier diffusion lengths (or equivalently the lifetime) and the surface recombination velocity at the grain boundary. Finally, more general uniformity investigations on polycrystalline silicon have been done [27,28].

A method for determination of the internal (columnar) series resistance in CIS and CIGS solar cells is reported in [15]. Since the region over which the light-generated current flows perpendicular to the junction is determined by the area of incident laser illumination, a variation of the spot size in turn changes the series resistance, R, by the relation:

$$R = \frac{\rho L}{A} \tag{2.2}$$

where ρ is the material resistivity, L is the length over which the current flows, and A is the illuminated area. By making measurements of the AC photocurrent as a function of voltage with many spot sizes, the material resistivity can be extracted from the parameters that best fit the data. In this type of analysis, equivalent circuit modeling is generally used to generate curves for fitting of the data. A typical resistivity the order of 10^{-4} $\Omega\,\text{cm}^2$ is obtained for CIGS films. This type of result is important in separating efficiency losses due to resistance in different parts of the the cell. It is also an important parameter to be considered when evaluating the applicability of a particular material to concentrator technologies, where current densities and thus series resistance losses are vital issues.

Groups investigating CdTe thin film solar cells with focused laser beams have found a large dependence on intensity, but differ in their explanation of this observation. Reference [16] used spot sizes in the range of 30 to 500 μm, with collected currents the order of 500 mA. This represents incident power densities of several hundred suns at the smallest spot size. The voltage dependence of the collected AC photocurrent at various spot sizes became increasingly difficult to model with the smallest spot sizes, but all major effects were attributed to series resistance.

In contrast to reference [15], no fitting of the data was actually performed to extract the series resistance in reference [16]. Instead, the voltage offsets along a line of constant current were extracted for different spot sizes; the voltage offset divided by the current gives the effective resistance. A value of 0.024 Ω cm^2 was extracted in this way for the columnar resistivity of CdTe. This method assumes that the local junction voltage at the illumination point is higher than the measured cell voltage. This is due to the (reverse) photocurrent flow through the series resistance, which leads to a voltage drop. If one assumes the potential is constant throughout the top and back contacts, this voltage drop must result in a local increase in junction voltage.

These assumptions are not necessarily valid. Firstly, at the current where the voltage offsets are measured, ohmic resistance may not be the only effect leading to the offsets. Intensity dependent recombination effects, as well as conduction barriers due to the nature of the heterojunction interface may be present. Secondly, losses in the collected photocurrent may result from the large non-illuminated diode in parallel with the illuminated region, as well as from the measurement circuit itself [29]. Finally, and most importantly, the incident AC illumination will be shown to modulate the forward current of the illuminated portion of the diode, since the voltage drop across any series resistance will drop to a minimum as the modulated laser intensity drops to zero, in turn changing the diode junction voltage. This will result in a partial cancellation of the collected signal.

The work represented by references [17–19] does not examine the voltage dependence of the collected photocurrent in detail. Instead, the dependence of contrast on intensity at zero bias, as well as the dependence on post-deposition processing, is examined. Increased contrast under high illumination was explained as being due to poor collection efficiency under high injection conditions. It is likely that a portion of the increase in contrast at high intensity is due to variations in junction performance at high injection; however, resistive effects will be shown to be a more dominant effect. It is also suggested in related work that the increase in contrast may be due to variations in depletion width due to doping gradients in the material and near grain boundaries [30].

The majority of information on LBIC in the literature is based on measurements done on polycrystalline silicon. However, it is in general not possible to directly apply the type of analysis used for polycrystalline silicon to thin film cells. The calculations of the response near a grain boundary cannot be easily applied to thin film polycrystalline devices for two main reasons. Firstly, for the calculation to be straightforward, the dimension of illumination (the spot size) must be much less than the grain size. The diffraction-limited spot size for the far-field technique of ~0.5 μm is usually too large to fulfill this condition for CdTe and CIGS grains. Secondly, the large number of defect energy levels complicates the recombination paths at the grain boundary, and does not allow the assumption of a single surface recombination velocity.

2.5 Summary

While the application of LBIC to polycrystalline thin film solar cells has been explored by various groups, it is not used at this time for routine cell characterization. Part of the barrier to applying this technique has been the interpretation of the data. As noted in this chapter, intensity and bias dependent effects can lead to misleading interpretations of the data.

It is clear that specific, reproducible methodology needs to be applied to avoid ambiguity of interpretation. Techniques developed by others include using varying spot sizes to measure the columnar resistivity of the absorber and modeling the equivalent circuit with software such as Pspice. Bias and intensity effects have also been previously explored, but without a great deal of quantitative analysis. It is noted again that the theoretical and measurement techniques developed for polycrystalline silicon-based devices often cannot be directly applied to the materials in this study.

The goals set for the apparatus at Colorado State University were micron resolution, high sensitivity electronics (1 sun equivalent illumination at the highest resolution), and a repeatable positioning system to allow for direct evaluation of light and heat stress effects on local areas. These goals have been met by the current system. The key issue is reproducibly controlling the light intensity and spot size, so that comparisons may be made both between different types of devices and between the same device after exposure to light and/or heat stresses.

The apparatus at Colorado State also features several enhancements over other similar devices. The power at the sample is monitored, allowing for the collected current to be expressed in terms of the apparent quantum efficiency. This allows quantifiable comparisons to be made between measurements. It is also essential for comparisons of the effect of a parameter such as intensity to be made; comparing the contrast alone will not indicate if the mean response is changing.

In addition, the system is capable of using multiple laser wavelengths, which allows one to separate issues of light intensity through the ability to control the generation volume. This capability may also be helpful for evaluation of the uniformity of diffusion lengths and local bandgap variations due to preferential alloying at specific sites (such as grain boundaries).

Chapter 3

Description of Experiment

The laser stepping apparatus was constructed to measure the spatial uniformity of solar cell response with very high resolution. The initial goals were to (1) achieve a diffraction-limited spot size (~1 μm), (2) measure photocurrent at low enough levels so that when using the most sharply focused beam, photon densities are close to "real-world conditions", i.e. 100 mW / cm^2, and (3) map a solar cell, remove it from the apparatus to subject it to heat, light, or other environmental stress, subsequently replace it in the apparatus, and return to the same position within ± 1 μm.

The apparatus consists of three sub-systems: optics, positioning equipment, and electronics. The first two are shown schematically in Figure 3.1. The optics system consists of laser diodes coupled with single-mode fibers, a collimating lens, an optical chopper, a polarization optic, a beam sampler, a laser power attenuator, beam steering mirrors, and a high quality microscope objective with adjustable compensation for focusing through

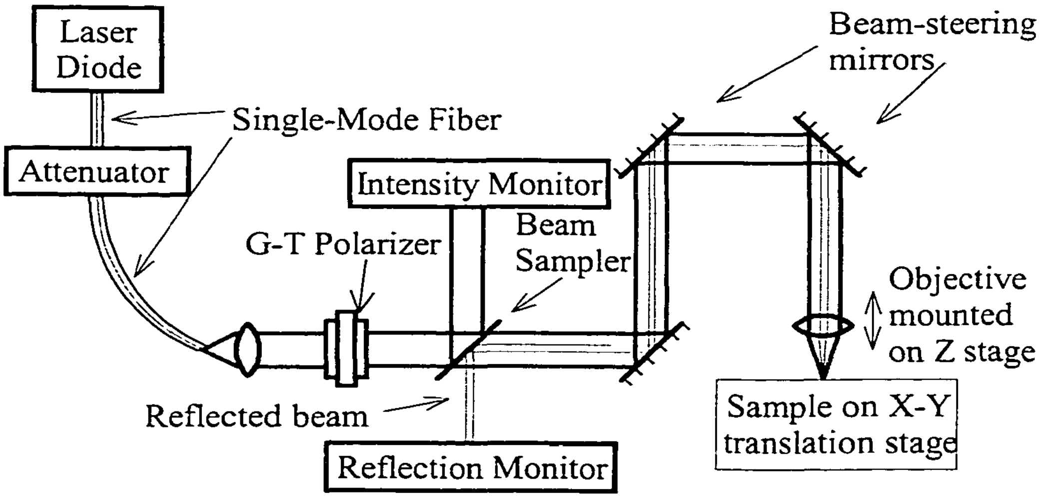

Figure 3.1. Schematic of apparatus.

glass. The positioning equipment is made up of three identical high resolution computer controlled translation stages, each with repeatability and backlash control better than 0.5 μm. The electronics setup has a current-to-voltage amplifier and a lock-in amplifier at its basis. In addition, extensive Labview® software control has been developed to integrate positioning and electronics. The setup allows full control of experimental parameters from a single screen on the monitor.

3.1 Optics System

3.1.1 Laser Diode Controller

A Thor Labs LDC500 laser-diode controller was selected for the stability of its current supply and its compatibility with the laser diodes themselves. The controller also allows the lasers to be intensity-modulated. With intensity modulation, the light need not be mechanically chopped to achieve an AC component, and hence there is less noise at the detection frequency, resulting in an overall better signal-to-noise ratio. An oscilloscope is used when choosing appropriate parameters for modulation, since the waveform quality can depend on many factors. The laser can be modulated in constant current or power mode. Both modes are used, depending on which gives the best performance for a particular laser. The output current or power is controlled to given by:

$$I_{LD} = I_{LDset} + I_{LIM} \cdot \frac{V_{MOD}}{10\ \mathrm{V}}; \quad I_{PD} = I_{PDset} + 0.2\,\mathrm{mA} \cdot V_{MOD} \tag{3.1}$$

where I_{LD} is the current output in constant current mode, I_{LDset} is the laser diode current setting in constant current mode, I_{LIM} is the current limit, I_{PD} is the photodiode current (monitors the laser diode output), I$_{PDset}$ is the current setting in constant power mode, and

V_{MOD} is the modulation voltage at the BNC connector. See Figure 3.2 for the output of one laser as I_{LDset} is varied. Figure 3.3 shows the modulated laser output resulting from different values of I_{LDset}. The operating point is usually chosen to yield a modulation which has a minimum near zero emitted power. However, this configuration allows the flexibility of choosing different amounts of DC offset laser illumination, which may be useful for examining the effects of local light biasing.

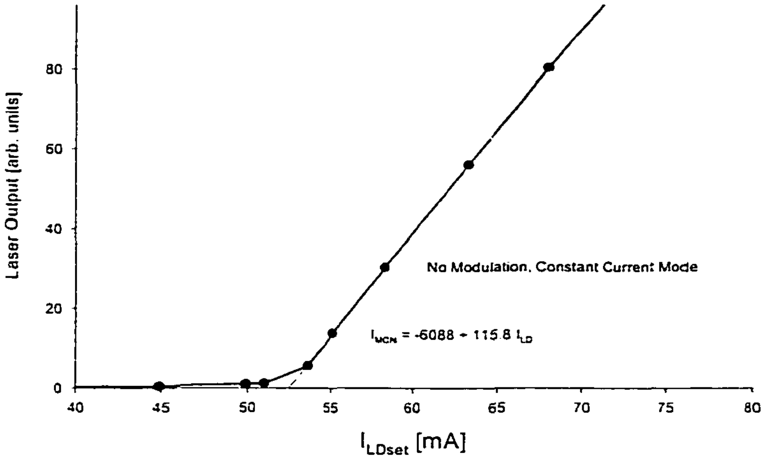

Figure 3.2. Laser diode output as a function of operating point.

The warm-up time and stability of the laser output are shown in Figure 3.4, where the AC component of the output has been measured at both the sample position and the monitor position. Initially the laser output varies the order of 1 percent, but after a warm-up time of about 5 minutes, variations are reduced to less than 0.2 percent. The sample electronics, which measures the device current, (dotted line in both graphs) shows slightly better noise performance than the monitor electronics, which measures the laser power. This is mainly due to the lower power available to the monitor photodiode (due to the 90/10 ratio beam splitter). The noise level, however, is in this case much less than the variation in laser output power.

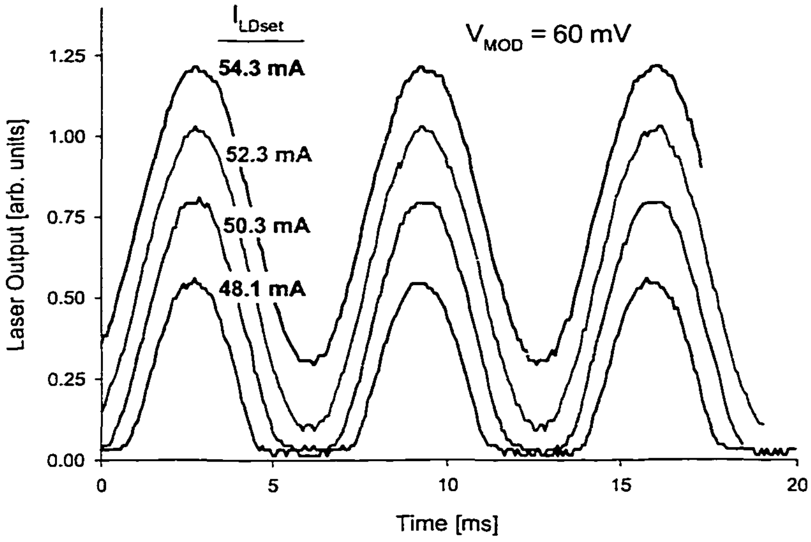

Figure 3.3. Modulated outputs resulting from different laser operating points.

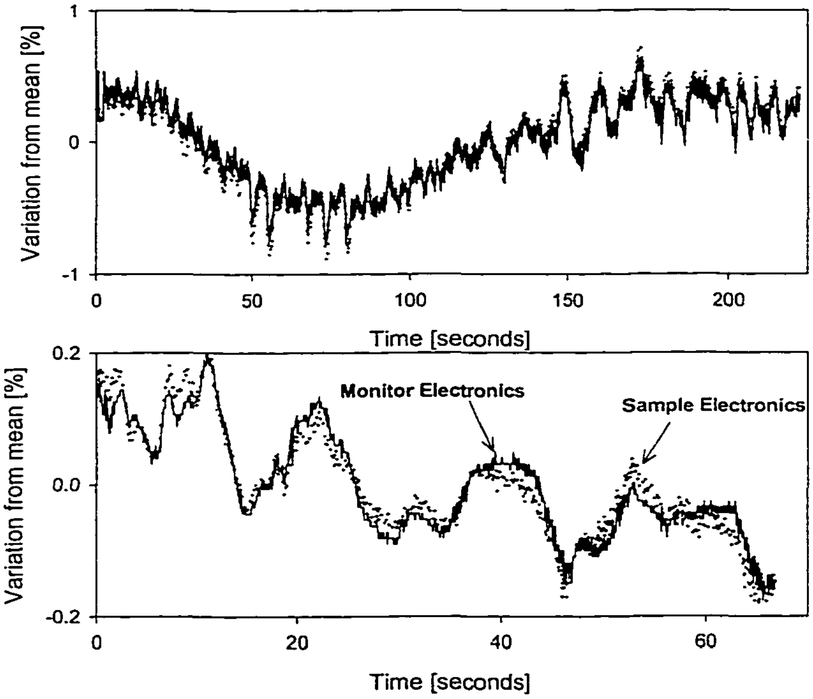

Figure 3.4. Graphs illustrating the warm-up time (top) and stability (bottom) of the lasers. Note the different scales used.

Table 3.1. Settings used for lasers in experiment.

Wavelength [nm]	I_{LDset} [mA]	I_{LIM} [mA]	**Mode**	**Min. Attenuation [dB]**
638	-49.1	74.6	Const. Power	5
685	48.3	76.0	Const. Current	0
788	38.4	63.6	Const. Power	11
823	38.8	95.0	Const. Power	9
825	9.8	50.4	Const. Power	1
830	10.7	50.4	Const. Power	1
835	11.3	50.4	Const. Power	1
840	12.3	50.4	Const. Power	1
845	13.1	50.4	Const. Power	1
850	14.4	50.4	Const. Power	1
855	15.6	50.4	Const. Power	1
857	16.0	50.4	Const. Power	1

Figure 3.4 shows that it is possible to correct for changes in power at the sample by simultaneous measurement of the power at the monitor position (see Figure 3.1). However, this leads to an increase in the effective noise in the measurement, and when the beam power is low the variations due to noise in the intensity monitor signal can be much larger than the measurement noise. For this reason, the beam power is measured, but no feedback is given to the intensity attenuator. Instead, subsequent analysis can correct for changes in the beam power, generally by smoothing the intensity-monitor signal.

The settings used for each of the laser wavelengths are shown in Table 3.1. The wavelength range 825-857 nm is covered by one laser diode by cooling the diode, as described in Section 3.1.3. A modulation voltage of 60 mV at 151.51 Hz is used for all lasers.

3.1.2 Fiber-Coupled Laser Diodes

Laser diodes were chosen over a HeNe laser partly because of the relatively low cost of having multiple wavelengths (only one controller for many lasers need be purchased), but primarily because of the superior beam characteristics obtained from a single-mode fiber. The small fiber core excludes all but the Gaussian TEM00 spatial mode, ideal for focusing a beam down to a minimum spot size. Additional lasers can be added to the system as needed. The laser diodes have typical output powers of 1-10 mW from the fiber. Such power is more than sufficient, which allows extra flexibility in monitoring the laser and coupling all lasers into a common fiber.

A particular laser diode is selected by connecting its output fiber to the input fiber of the attenuator. This is accomplished using a simple feedthrough component. It is a very simple way to switch lasers, but has the complication that the coupling efficiency and output polarization depend on the relative rotation of the patchcord fiber to the laser output fiber, since s- and p- polarizations travel perpendicular to one another in each fiber core. The beam splitter and mirrors have different reflection coefficients for s- and p- polarization; this results in changes in the reflection as the fiber coupling is removed and replaced. Therefore it is necessary to include an optic which transmits only one polarization to the rest of the experiment, as discussed in Section 3.1.7.

The various laser diode wavelengths used in the system are shown in Figure 3.5, with the CdTe solar-cell quantum-efficiency curve from Figure 2.2 shown for reference. 635, 685, 780, 830 and 850 nm lasers were chosen both because of availability (none are readily available below 630 nm at a reasonable price) and to match the response of the solar cells under study. The actual output spectra of the lasers was measured using an Ocean Optics fiber-based spectrometer (IRRAD-2000). The actual center wavelengths and $1/e^2$ half-widths (in parenthesis) at room temperature after the lasers reached a stable output were 638.3 (2.1), 685.4 (2.1), 788.2 (2.6), 823.4 (2.3), and 857(2.5) nm. The 850 nm laser will be examined in more detail in the following section.

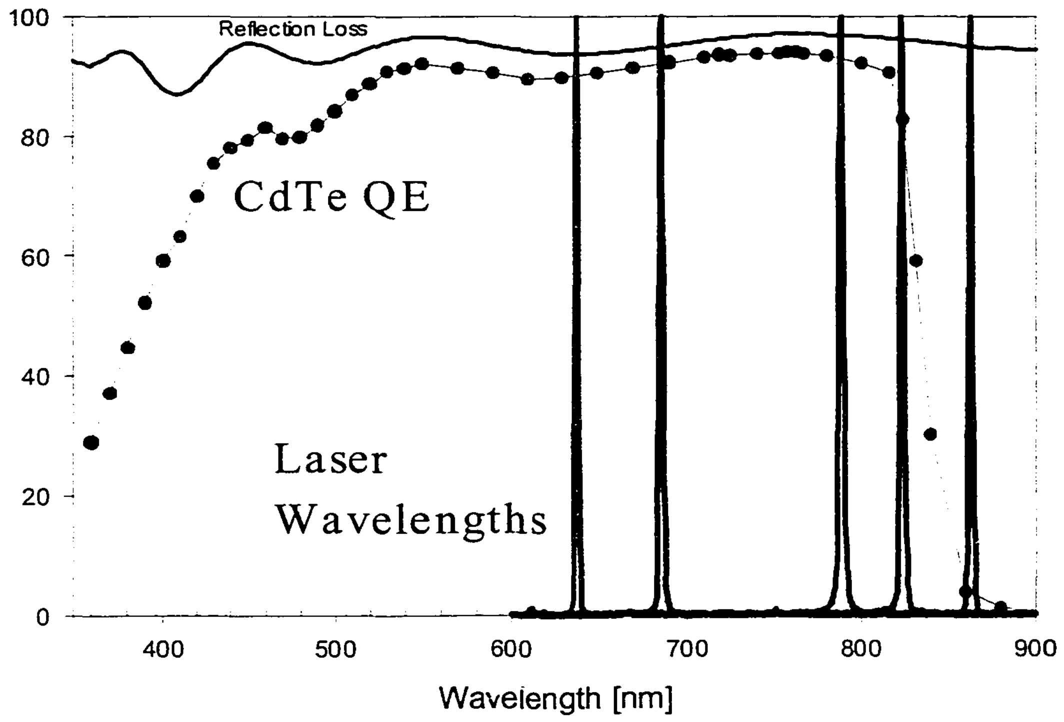

Figure 3.5. Quantum efficiency of a CdTe-based device shown the laser wavelengths used in the experiment.

3.1.3 Temperature Control of the Laser Diodes

Temperature controlled mounts for laser diodes are available commercially, using thermoelectric cooling. Temperature control reduces mode-hopping in laser diodes, essentially improving stability. In addition, temperature shifts the laser-diode wavelength the order of $0.2\,\mathrm{nm} / {}^{\circ}\mathrm{C}$. Since the lasers operate at relatively low power and thus produce little heat, ambient-temperature mounts with good heat-sink characteristics were used instead. Observations of the mount near the diode have indicated temperature rises during operation of less than 2 °C.

In addition, the 850 nm laser was fitted with a modified mount which allows the laser to be temperature tuned using a simple low temperature N_2 flow method. Since the bandgap of the laser (a quantum-well system) decreases with temperature, the lasing wavelength can be reduced by lowering the diode temperature. This technique is applicable to all the lasers. Monitoring of the laser diode temperature is not easily accomplished, because of the mounting system used for pigtailing the lasers. Instead, the output wavelength is monitored directly. As much as 80% of the laser light is not coupled to the fiber and the remaining light is scattered near the coupling point of the single-mode fiber to the laser. This scattered light can be continuously monitored with a spectrometer without disturbing the rest of the experiment. By controlling the rate of N_2 flow, the central wavelength can be controlled to within ±0.5 nm for extended periods of time (>10 min). Figure 3.6 shows spectra acquired during a data run, where the center lasing wavelength was varied from 850 to 830 nm. Note

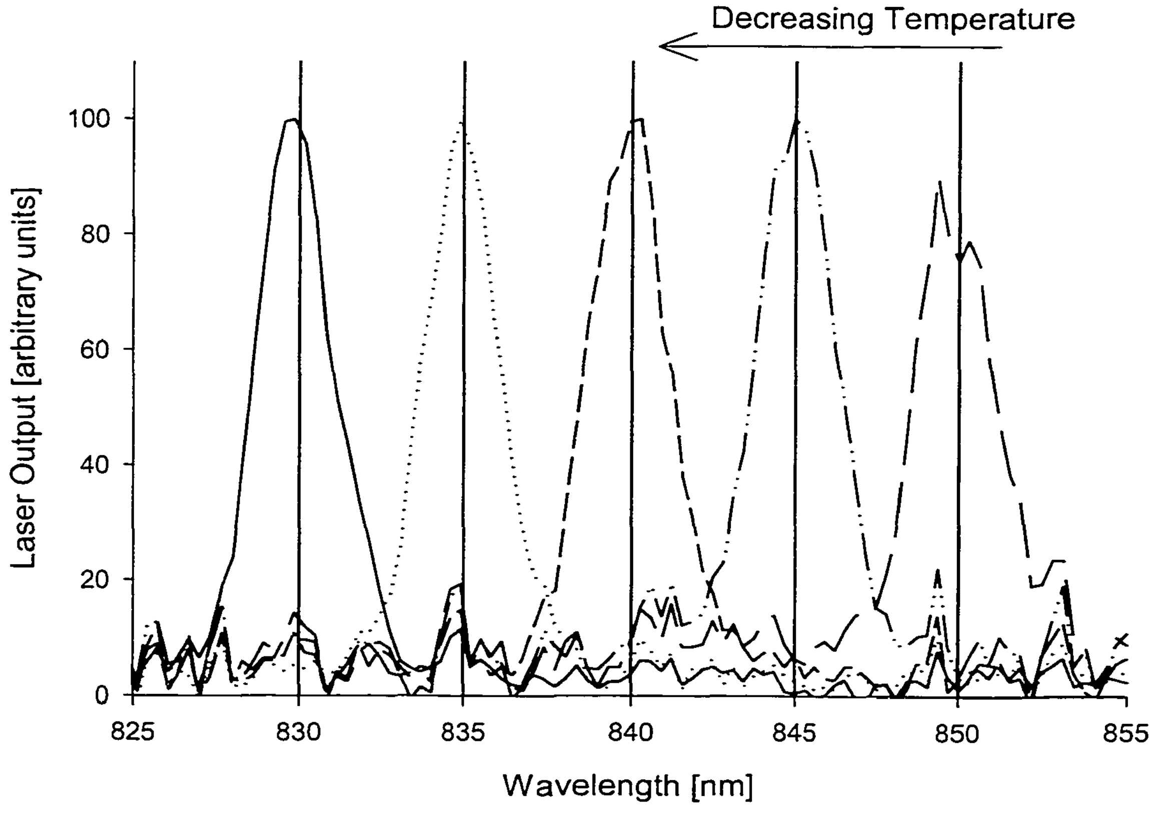

Figure 3.6. Laser spectra at different laser diode temperatures.

the half-widths of the spectra decrease with lasing wavelength from 1.2 to 1.5 nm. This variation does not have a significant impact on the results. The output power efficiency of the laser is also higher at lower temperatures, but this is compensated for automatically by the laser diode controller, which is operated in constant power mode.

3.1.4 Fiber Holder

The pigtailed laser diodes are fitted with FC style connectors. FC/APC is also available, and reduces back-reflections. Since this application is not very sensitive to back reflections, and FC/APC is not compatible with coupling into the FC patchcord of the attenuator, the standard FC style is used. Since collimation of the laser is a critical part of the optics system, the end of the fiber is held with a very stable, dependable mount (New Focus Model 9091). This mount allows 5 axes of adjustment of the fiber end (x,y,z,φ, θ).

3.1.5 Collimating Lens

The lens used to collimate the output of the fiber (essentially a point source of light) is a key component. A Gradium lens was chosen for its well corrected (for spherical aberration), achromatic (focal length changes minimally for wavelengths from 630 - 1000 nm) behavior. The focal length (20 mm) was chosen to produce a beam large enough to fill the microscope objective clear aperture. The collimated beam radius, w, is calculated from the numerical aperture ($N.A.$) of the lens (0.12) and the focal length (20 mm) as:

$$w = N.A. \times f = 2.4 \text{ mm} \tag{3.2}$$

The lens is quite sensitive to angular alignment, and a New Focus 9885 mount provides stable adjustment. Note that the collimating lens is plano-convex, and care must be taken to orient the lens with the plane side toward the fiber output to reduce aberrations. Figure

3.7 shows the near-Gaussian profile of a 830 nm collimated beam. It has a slightly larger beam radius compared to that predicted in equation 3.2, most likely due to modest non-optimization in collimation. Note that the overall performance of the optics system does not depend strongly on collimation, so that a non-optimized beam size is acceptable.

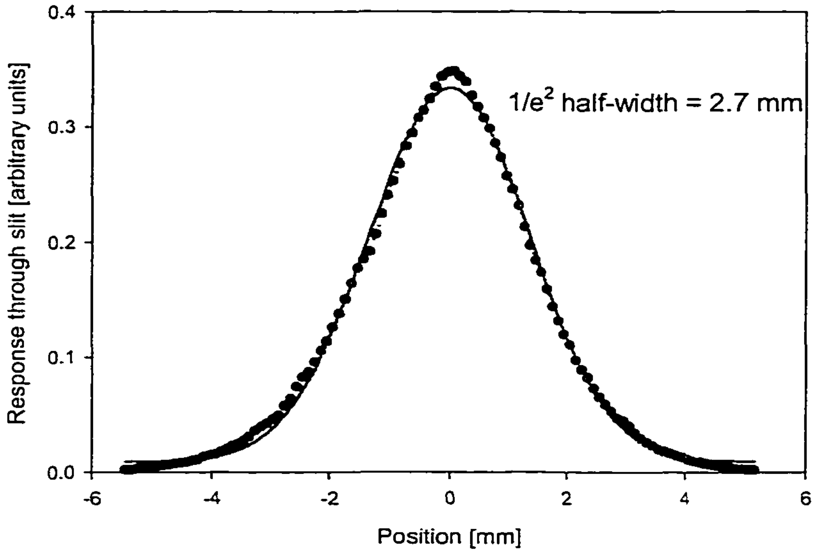

Figure 3.7. Example of beam profile after collimation.

3.1.6 Mechanical Chopper

The Stanford Research Systems (SRS) model SR540 mechanical chopper was selected. It is a standard model used by many labs. The chopper is needed for several reasons. Firstly, if a light source (such as a monochromator) which cannot be modulated electrically is used, one must chop the light to use phase sensitive detection. Secondly, electronically modulated light results in an AC signal on top of a DC light - the light does not in general go to zero at any time. Disadvantages of a chopper include poorer noise performance (due to vibration and jitter at the reference frequency) and that high frequency components inherent in a square wave may result in complications to the solar cell response. Whether to use the optical chopper or electrical modulation is evaluated for each type of measurement.

3.1.7 Polarization Optic

The polarization optic presents the beam sampler with a fixed polarization, regardless of the polarization coming out of the fiber. This is important since the reflectivity of the beam sampler depends strongly on the incident polarization. If the ratio of s- to p-polarization ratio changes, the calibration of monitor signal to power at the sample will change. More importantly, if the output polarization of the laser changes between the calibration and when data is taken (mode-hopping will likely affect the polarization), the transformation from photocurrent to quantum efficiency will be in error by an unknown factor.

The Glan-Thompson polarization optic consists of two calcite prisms cemented together. Because of the birefringence of the crystal, one orthogonal component of the arbitrarily polarized beam is transmitted, while the other undergoes total internal reflection at the interface of the two prisms, and is absorbed by the housing. As shown in Figure 3.8, rotation of the optic with respect to the incident beam results in passing different components of polarization. The choice of polarization determines the reflectivity of the beam sampler,

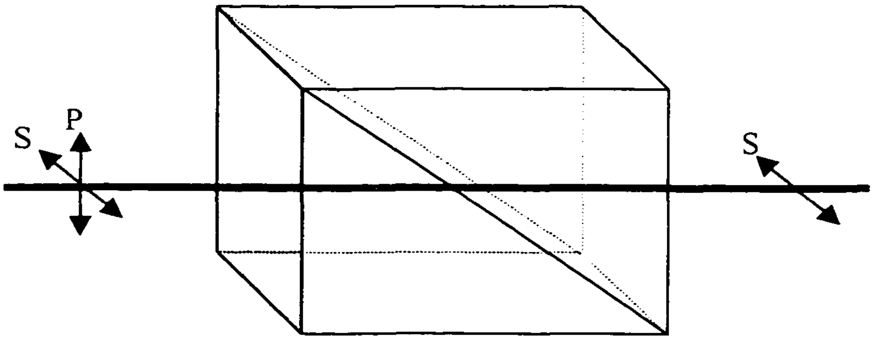

Figure 3.8. Glan-Thompson polarization optic.

which in turn controls the available range of laser powers at the sample, as discussed in Section 3.6.5.

3.1.8 Beam Sampler

The beam sampler reflects ~10% of the incident laser power and allows one to monitor the output power of the beam. As already stated in Section 3.1.2, the reflectance of the sampler is dependent on the incident polarization, as well as the wavelength. The beam sampler also functions to reflect a fraction of the light reflected from the sample to the reflection-monitor photodiode.

3.1.9 Fiber-based Attenuator

In order to controllably vary the spot size while keeping the incident power density constant, and to investigate the dependence of device collection efficiency on intensity, it is necessary to quantitatively control the incident power density over at least four orders of magnitude. One option is to use neutral density filters. Problems with these filters, however, include introduction of additional multiple reflections and reduction of the beam quality. In addition, the filters reduce the transmitted power in discrete amounts and must be adjusted by hand, which necessitates disturbing the apparatus to some degree. This last two issues are primarily problems of convenience, but the latter would significantly increase the difficulty of use of the apparatus.

Each of these issues is addressed by the use of a fiber-based, digitally-controlled optical attenuator (OZ Optics DD-100). The instrument comes with input and output single mode fibers, and attenuates the laser power by placing a variable blocking mechanism between the coupling points of the two fibers. The blocking mechanism consists of an opaque material with a sharp edge; the proportion of the beam blocked is varied by a computer-controlled (RS-232 interface) micropositioner. The amount of attenuation can in this way be varied over six orders of magnitude. Since the light is again coupled into a single mode fiber, the beam quality is unaffected, and multiple reflections that might strike the monitor photodiodes or the sample are not present. Finally, the power can be varied continuously by sending a command from the computer.

3.1.10 Mirrors / Beam Steering

MAXBRite/003 Mirrors were selected from Melles Griot for good surface quality (60-40 scratch-dig, $\lambda/10$ flatness) and excellent reflection (>98%) over the 630-850 nm wavelength range. The mirrors are one limiting factor in the wavelength range accessible to this apparatus. Since they do not reflect significantly below 630 nm, no blue or green lasers may be incorporated into the system without replacing the mirrors. Beam steering is provided by Newport components (670-RCT and 670-RCB), which feature excellent stability and very sensitive adjustments. Damped mounting rods are used to minimize vibration in the system.

Alignment of the beam to be collinear with the translation axis of the z translation stage is crucial to ensure that changing the spot size (by moving the objective in the vertical, or z-direction) does not affect the intensity delivered to the sample. Four degrees of freedom are required (x,y,θ,φ) and are provided by the two mirrors mounted above the sample. Alignment is accomplished in the following way:

1. A position-sensitive-detector (PSD - see Section 3.1.11 for details) is mounted to the objective holder. Care should be taken that the center of the quadrant PSD is aligned to the center of the objective holder.

2. The beam must be roughly aligned in both position and angle.

3. The translation stage is then moved up by its maximum travel and the beam is centered on the PSD using the first (in beam line) adjustable mirror.

4. The translation stage is moved down the maximum amount and the beam is again centered, but this time with the second adjustable mirror (directly above the objective).

5. The stage is moved up and the beam position is over-corrected with the first mirror and moved to the center of the PSD with the second mirror.

6. The stage is moved down and the beam is centered on the PSD with second mirror only.

7. Steps 5 and 6 are repeated until beam is centered on the PSD at all z positions. To avoid confusion, the direction all four knobs must be turned (cw or ccw) is identified and only turned in one direction. Relatively small over-corrections are used in step 5.

The beam should also be aligned to the optical axis of the microscope objective. In practice this is very difficult, since a mount for the objective should be designed to be goniometric - the center of the objective should not move when it is tilted. When the optical axis is not aligned, the beam emerges at some unknown angle to the z translation axis, resulting in the x-y beam center position changing with spot size. This can in principle be compensated with software, but likely is not an issue when the angle is small enough. The minimum spot size, however, will be compromised if the beam is not very nearly parallel to the optical axis.

3.1.11 PSD / Quadrant Detector

A UDT quadrant detector (Spot-9DMI), a silicon photodiode segmented into four quadrants, each isolated electrically, was used for alignment of the collimated beam to the translation axis of the z stage, as described in Section 3.1.10, and a transimpedance amplifier was designed and built. The four outputs are connected to the A/D inputs of the SR810 lock-in. The relative position of the center of the beam is given by:

$$X = \frac{(A+D)-(B+C)}{A+B+C+D} \; ; \; Y = \frac{(A+B)-(C+D)}{A+B+C+D} \tag{3.3}$$

where A, B, C, D are the voltage outputs of the four quadrants (labeling clockwise).

3.1.12 Other Detectors

To quantify beam intensity power, two UDT sensors (PIN-DP) were purchased and calibrated at NREL (NIST traceable external quantum efficiency). Data files are available containing the quantum efficiency at 5 nm intervals. The power is then calculated from the output current as:

$$P = \frac{I}{QE}\frac{hc}{\lambda e} = \frac{I}{QE}\frac{6.625 \cdot 10^{-34}\,(\mathrm{J\,s}) \cdot 3 \cdot 10^{8}\,\mathrm{m/s}}{1.602 \cdot 10^{-19}\ \mathrm{C} \cdot 680\ \mathrm{nm}} = \frac{I}{QE}1.825\ \mathrm{W/A} \tag{3.4}$$

where I is the current and QE is the quantum efficiency at the lasing wavelength (0<QE<1). The software calculates the power based on the wavelength and quantum efficiency of the laser in use; the quantum efficiency and wavelength information are contained in the calibration files.

3.1.13 Microscope Objective

The Olympus 1-UB367 SL C PLAN FLUORIDE 40x/0.55 N.A. objective, equipped with a correction collar for focusing through 0 - 2.5 mm of glass, appears to be an ideal objective for this type of work. Its large working distance of 8.8 mm allows room for cell contacts. Spot size measurements indicate that its performance is near-diffraction-limited. Its clear aperture is 4.59 mm in diameter, which should be filled for best focusing performance. Note that if the objective is filled with light with a Gaussian intensity profile, the output will also be Gaussian. If the objective is filled with a uniform intensity, an Airy disc intensity distribution will be produced. Measurements of the beam profile indicate that a Gaussian profile is present both coming into and exiting the objective.

3.2 Positioning and Cell Mounting

3.2.1 Translation Stages

Three Newport MFN-25CC translation stages and a board-level MM2000 controller make up the computer controlled positioning system. Specifications and a tutorial can be found in the Motion Control catalog from Newport. The stages must be tuned for optimal performance, accomplished using LabView® software. Instructions for tuning can be found in the stage documentation. The stages are entry-level models from Newport, and advertise 1 μm repeatability and board level correction of backlash. Two of the stages were aligned at Newport to be orthogonal to 50 mrad.

The minimum reproducible step size at the present time is 0.2 μm, which is likely the smallest needed. Since the tuning parameters are dependent on the exact loading configuration of the stages, they should be independently tuned after any major changes. Data is taken step-wise; the stages must therefore reach their position and stabilize before data is taken. For this reason the software waits after the command to step the stages has been given. Wait times of 50, 80, and 250 ms are used for the typical step sizes used of 0.5, 5, and 50 μm. These wait times have been established by using the ability of the translation stage setup to report its position as function of time, which also has been implemented as a LabView® program. In the case of the lowest resolution data typically taken, where a

100 μm spot size is used and a 5x5 mm area is measured using step sizes of 50 μm, this wait time is the major component of the 45 min run time. Run times for smaller areas are progressively shorter, down to about 15 min for 50 x 50 μm regions.

Backlash of the stages and cell mounting hardware is the order of 0.3 μm, observed by translating the cell back-and-forth through where a feature in the photocurrent response is seen. Any change in the peak position indicates that the backlash is not correctly accounted for. By sending a command to the motion control board with the amount of observed backlash in each stage, this effect is automatically corrected.

3.2.2 Cell Mounting and Contacting

The geometry of the system setup presents challenges for contacting cells. Due to the limited size of the translation stages and the short distance which must be maintained between the objective and the top of the cell, custom cell holders were designed. Because of the need to replace the cells in a relatively repeatable manner, a set of rails (dowel pins) are used to mount separate cell holders, as shown in Figure 3.9. In this picture, the cell holder is directly below the microscope objective, and is shown mounted onto the rails, which are attached to the x-y translation stage setup. This method of cell mounting has several advantages: (1) The cell holder can be repeatedly positioned to within approximately 50 μm. (2) The reference cell used for calibrating the power at the sample position is permanently mounted in its own cell holder, which allows fast switching of the sample and reference cell. (3) Multiple cells may be contacted simultaneously using multiple cell holders.

A closeup of the cell holder is shown in Figure 3.10. The parts which slide onto the aluminum rails are machined from brass, which slides more easily on aluminum. The method of contacting a glass-substrate type cell is shown in Figure 3.10. In this case a small

Figure 3.9. Cell mounted in system.

set of leads contact the grid, and additional contacts to the back-contact are made with indium metal. All contacts are then connected to BNC connectors which are positioned close to the cell to minimize noise pickup. For glass-superstrate cells, contacts are made with spring-tipped probes, which are mounted on an adjustable stage. The cell is placed in the holder, and the adjustable stage moves up to contact the cell at four appropriate points. Two contacts are used for voltage sense and two for current read and biasing. The four-point probe method is used in both cases to avoid measurement of voltage drops due to contact resistance, since the voltage sense leads run very little current.

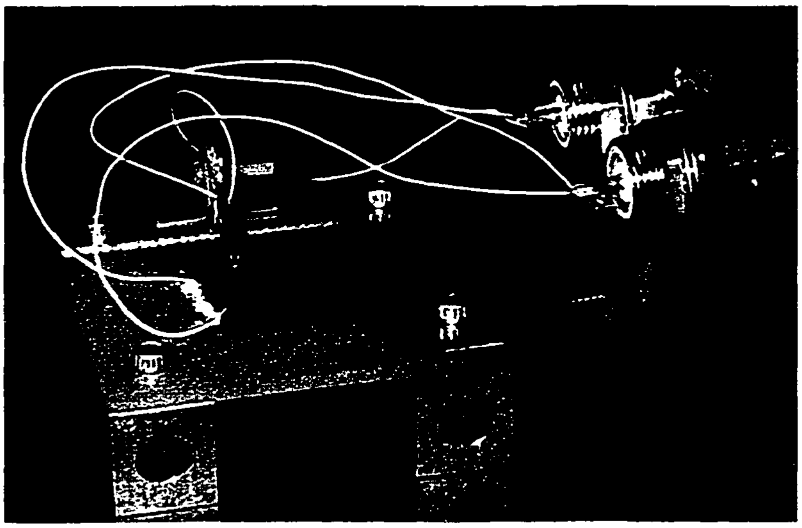

Figure 3.10. Closeup of contact method for glass-substrate type cells.

3.3 Electronics

3.3.1 Overview

Accurate determination of the photocurrent of solar cells in this context involves several complicating points. Firstly, the current to be measured varies over more than 5 orders of magnitude, corresponding to ~1 nA when a 1 μm spot size is used and ~10 μA for a 100 μm spot (assuming the incident power density is kept constant). The former very small current is extremely difficult to detect if care is not used. Secondly, measurement of the response while the cell is held in forward bias leads to a very small AC signal superimposed on the large DC current resulting from the forward current of the diode. This large DC current saturates the amplifier if it exceeds approximately 10 μA (for the gain setting typically used for bias-dependent data), unless one electronically subtracts this DC level.

Figure 3.11 shows a schematic of the electronics system. The DC voltage is measured via one set of contacts to the solar cell with a digital multimeter (HP 34401A), another set is connected to the SR570 transimpedance (I → V) amplifier, which includes a bias source. The output of the SR570 is connected to both the SR810 lock-in amplifier, which measures the AC component of the SR570 output, and another digital multimeter, which measures the DC component of the SR570 output.

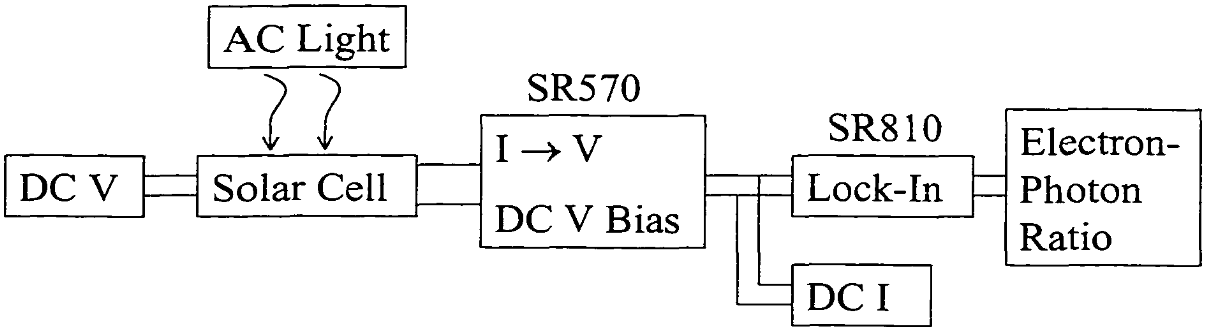

Figure 3.11. Schematic of electronics system.

3.3.2 Current Amplifier

Since the characteristics of the devices under study can vary, it is important to have good control over the input impedance of the current detection electronics to avoid changes in measured current because of loading errors. As shown in Figure 3.12, a 20 Ω input impedance will force a poor quality diode into forward bias, and the collected current (I_2) will be reduced from its value at zero bias because of shunting and series resistance effects. A Stanford Research Systems SR570 current-to-voltage amplifier allows device output at a virtual null bias (1 Ω input impedance for sensitivities $< 10\,\mu\mathrm{A}/\mathrm{V}$) or at a user-selectable bias from -5 to +5 volts. This allows the measurement to be made at an adjustable cell voltage. In addition, an input current offset is available to avoid overloading the amplifier with a DC offset current. Two RC filters with adjustable frequency cutoffs are also available. Specifications are included in the amplifier manual.

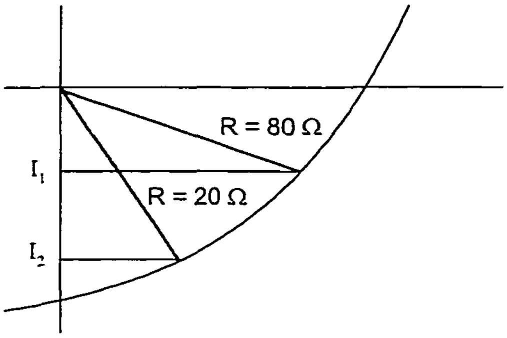

Figure 3.12. Effect of loading on photocurrent for a poor quality solar cell.

The sensitivity of the SR570 should be adjusted to produce ~1 volt RMS at the output when the maximum expected signal is present on the input. However, the frequency response and input impedance depend on the sensitivity setting. This can affect the measurement quite strongly, depending on the output impedance of the solar cell. Attenuation of the signal by a poor choice of sensitivity and/or filtering at a particular frequency is to be avoided. A safe setting for all solar cells investigated in this study is a sensitivity $\leq 500\,\mathrm{nA}\,/\,\mathrm{V}$. Higher sensitivities may attenuate the signal at the measurement frequency of 150 Hz. It also is extremely important to be aware of the changes in input impedance when the measurement is made with an applied bias. The input impedance will act as an effective solar cell series resistance, and affect the measured signal strongly. For this reason it is recommended that a sensitivity $< 10\,\mu\mathrm{A}\,/\,\mathrm{V}$ be used when making measurements with an applied bias.

3.3.3 Lock-In Amplifier

The output of the SR570 is measured by the Stanford Research Systems SR810 Lock-in Amplifier. The lock-in multiplies the signal by a sine wave at the reference frequency, decreasing the effective bandwidth to a fraction of a hertz. Since the SR810 is a dual-phase lock-in, both the part of the signal in phase and 90° out of phase with the reference sine wave (and thus the magnitude and phase of the signal) are available.

To ensure the best signal detection, the time constant (τ), sensitivity, and input parameters should all be optimized. The time constant minimum is determined by the signal frequency: τ is essentially how long the lock-in is looking at the signal, it is best to average over at least three cycles of the waveform. Therefore, for a 150 Hz signal, the time constant should be greater than 20 ms (30 ms was typically used). The time between readings should exceed 3τ for independent measurements. The sensitivity is easily set by sending an auto-scale command. The signal input should be set to AC - FLOAT, to eliminate coupling to ground. The magnitude of the signal is collected to eliminate phase shift errors as the sample is translated.

3.4 Cell Bias

In order to measure the voltage dependence of the collected photocurrent, the device under test is biased by the SR570 transimpedance amplifier. This is accomplished by biasing the input of the first-stage electronics to an adjustable internal voltage relative to ground. Since an applied forward bias will result in a DC current to be sourced from the solar cell, an equivalent DC current opposite in sign must be sourced to the input of the first-stage electronics (again internally to the SR570) to avoid saturating the amplifier. This is accomplished by measuring the DC current with a digital multimeter at the output of the SR570, and using a software-based feedback loop to null the total DC current by setting the magnitude and sign of the DC current sourced by the SR570.

3.5 Software Control

Labview® software has been developed to control all experimental parameters. Figure 3.13 shows the main window, with a one dimensional stepping scan of the measured photocurrent as a function of position (in this case as a sharp edge is translated through the beam at the focal point, resulting in a 0.8 μm measured spot size). Control of step size and other basic parameters are available on this window, others are accessed via clicking on various icons. In addition, other icons call sub-programs which allow the user to perform two-dimensional scans, photocurrent versus voltage measurements, etc. The software has been designed to generate immediate feedback, so that it is easy to keep track of where the beam is on the sample. The photocurrent can be measured as a function of position (with 1D or 2D scans), solar cell voltage, intensity, spot size, and time. Data and calibration files

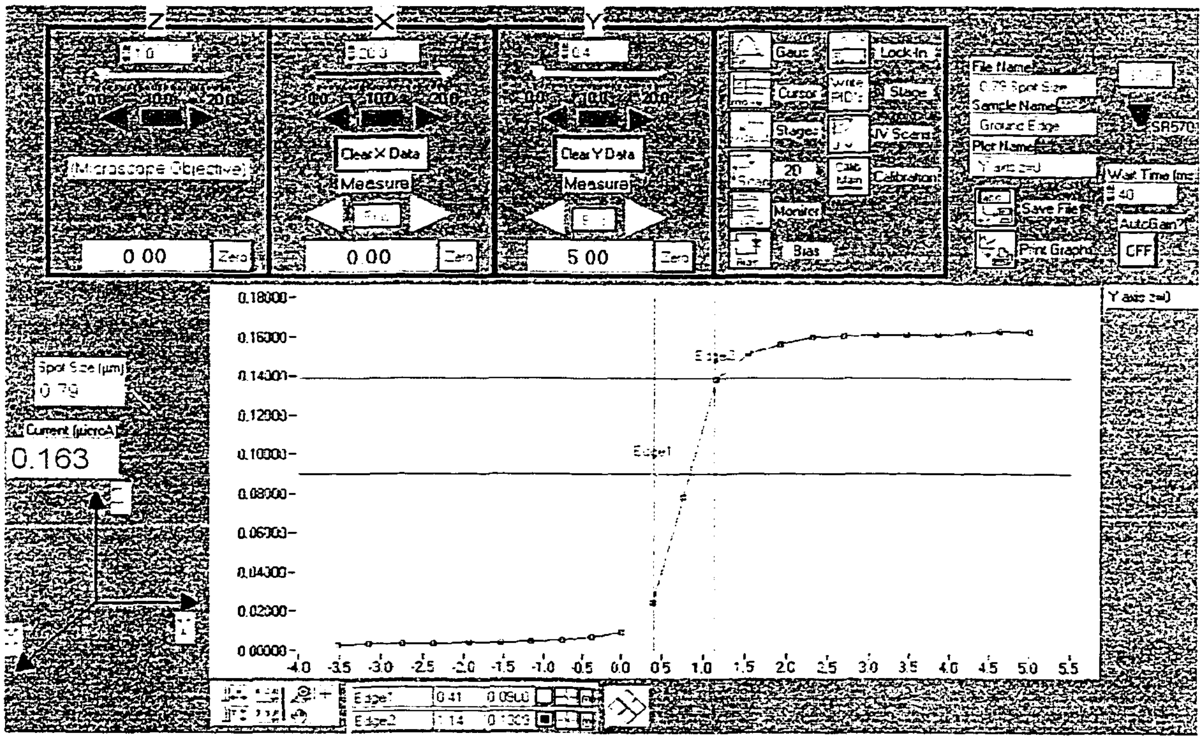

Figure 3.13. Experiment control software.

are generated automatically, usually for subsequent graphing using commercial software. The raw data is written to the file, with calibration data available both in the header and in separate files. This is important since user errors (such as incorrectly choosing the laser wavelength in the software configuration) would lead to incorrect reporting of the power density at the sample. With the raw data, the user can manually input the correct calibration data if necessary.

3.6 Experimental Considerations

The small-spot apparatus allows a wide range of measurements to be made on a cell in a reasonable amount of time under nominally controlled conditions. The details of the experimental setup are likely to have some effect on the data acquired; issues include background light incident on the sample (both from the lasers and the room background light), positioning repeatability, the accuracy of the measured values of current and position, and the calibrations made on various elements.

3.6.1 Background Light

The effect of background light on the solar cell response can be complicated. Incident light can populate traps, and the resulting photocurrent can affect both the solar cell response and the electrical circuit response. Background light at the reference frequency can introduce calibration errors, and can be introduced both at the sample and the monitor photodiode from multiple reflections of the laser beam. The use of electronic intensity modulation has the advantage of eliminating modulation of environment lighting sometimes associated with choppers. For these reasons the entire apparatus is covered with a dark rubberized fabric, and the ceiling lighting is turned off when data is taken. In addition, a cloth shields the sample from multiple reflections, allowing only light from the microscope objective to reach the sample. Background light reaching the monitor photodiode is reduced by the use of a long cylinder extended from the photodiode, which allows only collimated light to be detected. These precautions appear to be sufficient.

Incorporation of intentional background lighting at the sample has not been actively pursued. The electronics system can handle less than 5 mA of DC current, and noise is expected to become a problem if the entire cell is illuminated. One possibility is to offset the modulation of the laser by a DC offset, thereby increasing the injected carrier density. If a small modulation is used on top of the DC offset, circuit effects due to modulating the forward current of the diode will be changed. With a carefully chosen set of measurement conditions, it may be possible to separate intensity-dependent effects from circuit effects. This also may allow further exploration of trap states, and though not pursued in this thesis, it may be an interesting subject for subsequent work.

3.6.2 Positioning Repeatability

To make useful comparisons of the solar cell response under different conditions, it is necessary that the position of the incident laser beam with respect to the sample does not change appreciably. If the sample is removed and replaced, one must take more care in finding a reference point (such as a corner of the sample) to relate the before- and after-positions. The stages used specify position repeatability to ± 1 μm, and their observed behavior has exceeded this.

The use of multiple laser wavelengths introduces the question of whether the position of the spot on the sample changes with different wavelengths. All lenses in the system

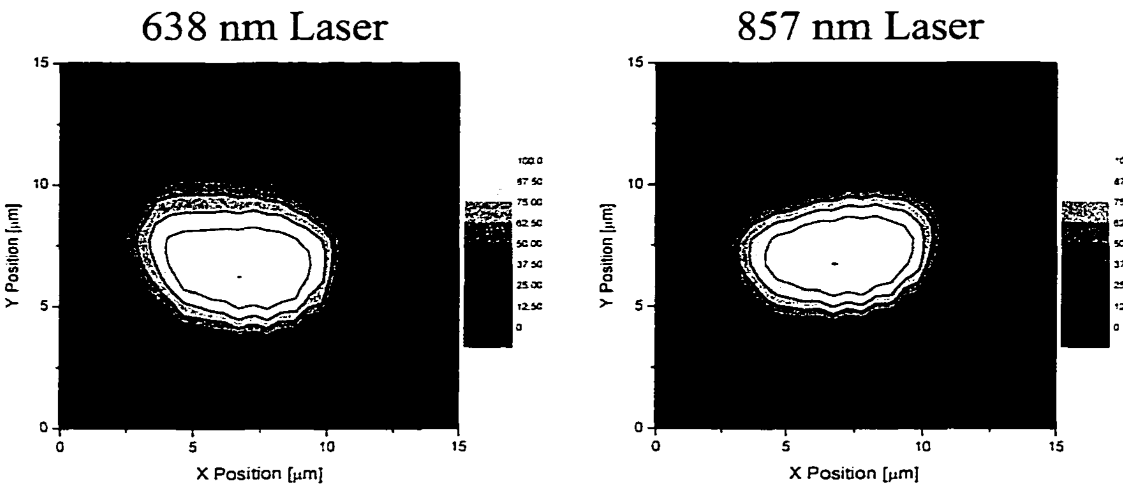

Figure 3.14. Normalized laser power through a 5 micron pinhole for two lasers, illustrating the repeatability of the spot size and position.

are achromatic, so that the change in focal length with wavelength should be minimal, and hence changes in the spot position should be minimal. To verify this assumption, a pinhole was placed above a photodiode mounted in the sample position, the spot size was minimized with one laser wavelength, and the pinhole was then 'imaged' with each laser under otherwise identical conditions. Figure 3.14 shows the results for two of the lasers, with center wavelengths at 638 and 857 nm. Measurements taken with other lasers show similar results. It is apparent that the repeatability is quite good. Analysis shows that the inferred position of the center of the pinhole is within $\pm 0.5\,\mu m$ for each of the lasers. The similarity in the gradient from zero power to the maximum power shows that the differences in the spot size and profile are likewise minimal.

3.6.3 Accuracy of Reported Values

Several experimental techniques are used to ensure that the reported values of photocurrent are accurate. Most important is the use of calibrated (NIST-traceable) silicon photodiodes to both monitor the power and calibrate the power at the sample position versus the measured signal at the monitor position. Secondary concerns include the effects of reflections at the sample, the effect of input impedance of the transimpedance amplifier, and the gain accuracy of the instrumentation used to perform the measurements. This concerns will be examined in the following sections.

3.6.4 Reflections

The results presented in this thesis are typically plotted in terms of the apparent quantum efficiency (AQE). This is done primarily because of circuit effects which affect the collection, particularly in forward bias. However, a secondary concern is that reflections, which reduce the power incident at the absorber, need to be taken into account. The collimated spectral reflection (see Section 3.6.5) is used both to find the plane of the sample with respect to the incoming beam, and to measure local variations in the reflectivity with high resolution, which could correlate with spatial variations in the collected photocurrent.

When glass superstrate devices are used, major reflections can occur both at the air-glass interface and the glass-TCO interface. Considering the first, since the beam is incident on the absorber near the focal plane of the lens, the spot size at the air-glass interface is always much larger than the spot size on the absorber. Thus local variations in the collected photocurrent with spatial size the order of the spot size cannot be caused by spatial variation in the reflectivity of the glass. However, since the TCO layer is typically less than 1 μm thick, reflections occurring at either surface of the TCO can be responsible for spatial variation of the photocurrent. Bias and intensity dependence (or a direct measurement of the reflection) must then be used to separate the causes.

It is important to note, however, that large variations in reflectivity would be necessary to account for significant photocurrent variations. The variation in reflectance R needed to produce a 10% change in the photocurrent is given by

$$|\delta R| = 0.1(1 - R) \tag{3.5}$$

so that, for a typical reflectance of 10%, $|\delta R| = 90\%$. In other words, the reflectivity must nearly double locally to result in a 10% variation in the collected photocurrent.

The last possibility for reflections affecting the collected photocurrent is reflections from the back surface, so that the light passes through the absorber twice or more. This is only a possibility for laser wavelengths which are very weakly absorbed by the semiconductor material, i.e. near the optical bandgap. Moreover, for the effect to be noticeable, the penetration depth must be the order of the absorber thickness. Since this occurs for an extremely narrow wavelength range, it is not likely to be a major effect, and can be separated by the use of multiple wavelengths near the bandedge.

3.6.5 Calibrations

Several calibrations are performed to ensure that reported results are accurate, the most important of which is the calibration of the monitor photodiode versus laser power at the sample. The spot size and plane of the sample are also calibrated. The calibration of spot size gives the distance from the focal plane for a particular spot size. Measurement of the sample plane ensures that the spot size is held constant as the sample is moved under the incident laser. Knowledge of the spot size is important for both modeling parameters and knowledge of the incident power density.

3.6.5.1 Power at the Sample

The polarization optic, beam sampler, and attenuator must be optimized together to set the desired power range available at the sample. Changing the rotation of the polarization optic will result in different reflectivity of the beam sampler, since one is changing the incident beam polarization. The range of reflectivity typically ranges from 2–10% for pure p- and s-polarized beams, respectively. This will directly affect the available power densities at the sample for the various spot sizes used. While the attenuator has 60 dB of range, the useful beam power range is limited by the fixed-gain transimpedance amplifier used for the monitor photodiode. The electronics saturate at 10 V, and the noise level is at $\sim 0.01\,\text{mV}$, leading to acceptable uncertainty in the measured power the order of 1% at a measured voltage of 1 mV. This limits the power range to a span of about 40 dB.

The choice was made to use the s-polarization state, which is maximally reflected by the beam sampler, in order to decrease noise in the power measurement when data is taken with a 1 μm spot size at 1 sun equivalent illumination. This limits the available power density at the largest spot sizes slightly. Figure 3.15 shows calibration data for each of the lasers. It also shows that with the current setup, the maximum power at the sample is limited to the order of 10 mW / cm^2 (0.1 suns) for a 100 μm spot. Data can still be taken at higher incident power densities, but the monitor photodiode electronics will be saturated, and one cannot independently measure the incident power.

With the polarization optic in place, variations in output power of the laser or changes in polarization do not affect the calibration, and one set of calibration coefficients is valid for each laser wavelength. To verify this, calibration of the monitor voltage versus power at the sample was performed before and after the fiber coupling was removed and replaced. A change in output polarization was evident in that the power at both the sample and monitor position changed. However, the calibration was unchanged to within ±0.5%. This value is typical for calibrations repeated over long terms.

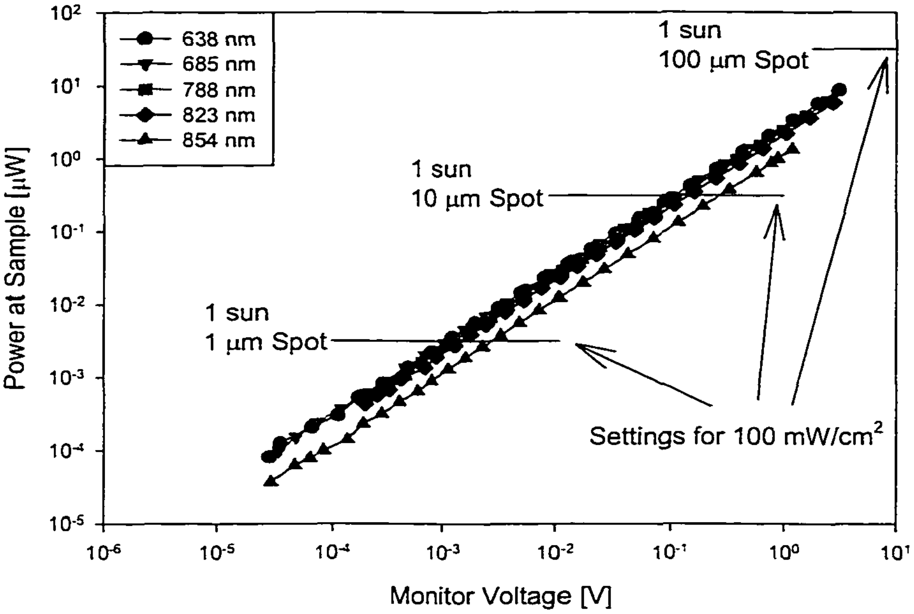

Figure 3.15. Power calibrations for all lasers used in the experiment. Shown for reference are the power used for 1 sun conditions at various spot sizes.

Since a log-log scale is used in Figure 3.15, the intercept is just the logarithm of the constant relating the power at the sample to the power at the monitor position. A graph of the calibration ratio versus lasing wavelength then gives an idea of how independent the system is of wavelength. Figure 3.16 shows that there is a range of about a factor of 2.5 in the wavelength dependence of the calibration, due to wavelength dependence of both the mirror reflectivity and microscope objective transmittance. This variation is consistent with reflectivity values given by the manufacturers.

3.6.5.2 Spot Size

The beam emerging from the microscope objective can be characterized using a razor blade, a slit, or a pinhole. The razor blade is the easiest (it can be taped above the sample) but one must differentiate the scan to get the beam profile. Also, the razor blade is good for

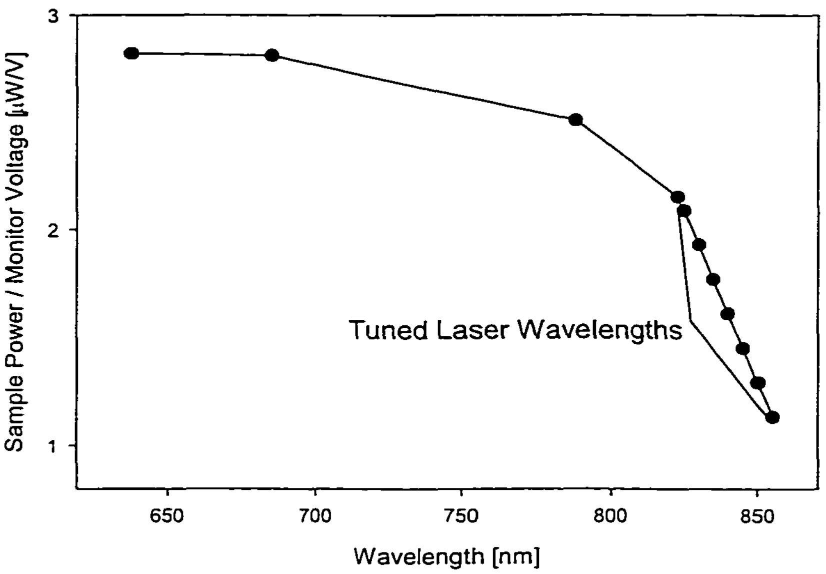

Figure 3.16. Calibration ratio from Figure 3.15 for each wavelength used in the experiment. The falloff is likely due to increased reflectivity of the microscope objective.

all ranges of spot size, though edge structure at the micron level can lead to measurement errors at the smallest spot sizes. A custom ground knife edge reduced the edge structure somewhat. A slit is a good option if a direct profile is desired, and one is interested in spot sizes large compared to the slit width. A pinhole is used when two-dimensional imaging is needed. Figure 3.17 shows a typical beam output as a function of the position (Z) of the objective. Note the depth of focus, the length over which the spot size is at its minimum, is ~5 μm.

The minimum spot size observed with zero correction has been as small as 0.7 μm. With the correction collar, a 1 μm spot has been achieved at λ = 680 nm after the beam has gone through 1.4 mm of glass. The theoretical minimum spot size for a 630 nm laser wavelength with the objective used is given by:

$$w_{Min} = \frac{\lambda}{2\pi\, N.A.}\frac{\phi}{w_o} = \frac{630 \text{ nm}}{2\pi 0.55}\frac{4.59 \text{ mm}}{2.4 \text{ mm}} = 0.35\ \mu\text{m} \tag{3.6}$$

where ϕ is the clear aperture of the objective and w_o is the radius of the incoming beam.

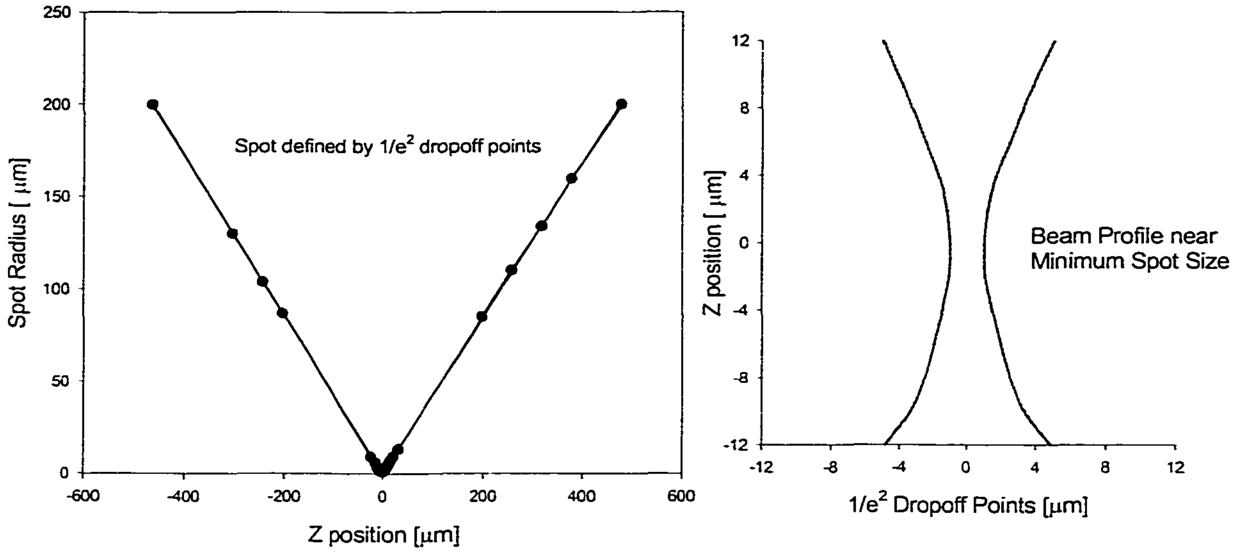

Figure 3.17. Example of beam profile used to calibrate spot size versus objective height.

Calibration of the spot size was accomplished by placing a sharp edge over a reference photodiode and measuring the spot size as a function of objective height. The spot size changes linearly with height until near the focal plane. A fit to the data away from the focal plane allows the spot size to be reported in real time to the user, once the position of the focal plane relative to the sample has been determined. Given the micron-size structure in most devices, this is easily accomplished by maximizing the contrast between high and low responding regions in a line scan. This calibration is expected to be valid as long as the optical system is not perturbed strongly enough to cause changes in the beam alignment to the microscope objective.

3.6.5.3 Sample Plane

If the sample is tilted with respect to the incoming laser beam, changes in the x-y position of the sample will result in unintentional changes in the spot size. To correct for this effect, the collimated spectral reflection is measured as a function of the objective-sample distance (z position). As shown in Figure 3.18, if the reflecting surface is farther

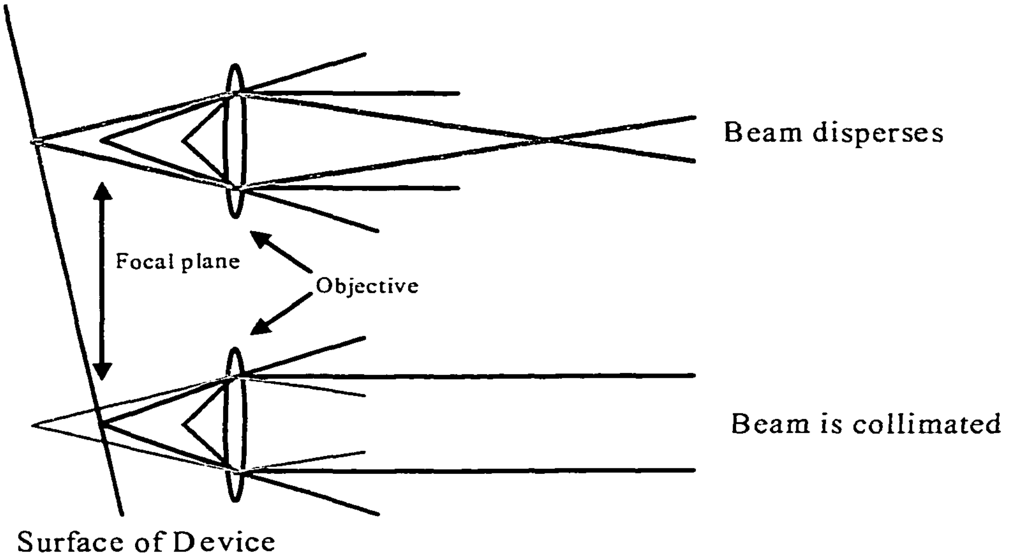

Figure 3.18. Illustration of collimated spectral reflection technique used for measurement of sample plane tilt.

from (or nearer to) the objective than the focal plane, reflected light will be dispersed by the objective. Since the reflection monitor photodiode is physically far from the objective, very little signal results. However, if the reflecting surface is near the focal plane of the objective, the reflected light is collimated, and the reflection monitor photodiode receives a reasonable proportion of the reflected light. The transition from minimal signal to the maximum is very dependent on z position, as shown in Figure 3.19. Extracting points of constant response gives z positions of constant spot size at various positions on the sample. The data is fit to a plane, and the parameters are used by the computer software to automatically correct for the tilt in the sample during subsequent measurements.

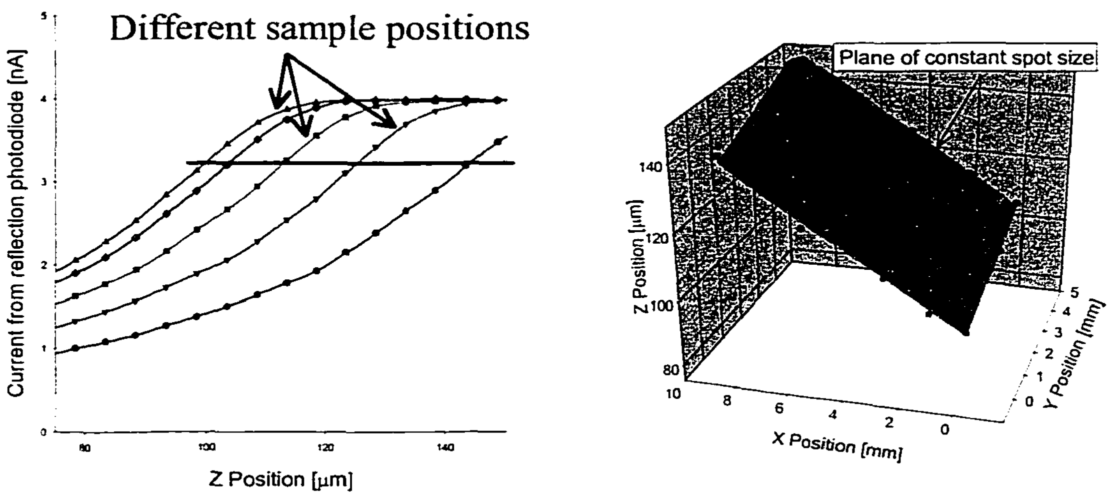

Figure 3.19. Method of correcting for sample plane tilt (left), and typical result (right).

3.7 Summary of Apparatus

The apparatus developed and described in this thesis is essentially a complete system, where all of the controls (aside from switching the fiber coupling to change lasers) are available through the computer interface. Data can be taken semi-automatically – once the area to be scanned, the laser spot size and power, and the sensitivity setting to be used have been specified, the program automatically measures the photocurrent and monitor voltage, as well as the actual stage positions of every data point, and writes the data to a file. The data can be graphed interactively with Labview programs written specifically for this purpose, or other graphing packages can import the data for analysis and graphing.

A suggested modification to the system is the incorporation of all lasers into one fiber simultaneously. This could be currently accomplished, but only with a complex optical system, utilizing multiple dichroic beam splitters, etc. It is expected, however, that advances in optical fiber technology in the next years will make this possible with fiber-based combiners, which are currently available for operation with laser wavelengths used in the telecommunications industry (1310-1550 nm). In addition, more ambitious projects might include extending the capability of the apparatus to include photoluminescence and/or direct measurement of the diffuse reflection.

The advantages of this technique over those such as electron beam induced current (EBIC) and near-field scanning optical microscopy (NSOM), which both also map carrier collection, are: (1) the reproduction of normal operating conditions, (2) ability to map an entire research-size sample, (3) ability to focus through glass, and (4) spatial location repeatability. Disadvantages include: (1) lower spatial resolution (cannot in general distinguish details of single grains), and (2) cannot give topographic information. This considerations suggest that the application of this technique would be aided considerably by EBIC and/or NSOM investigations of the same sample.

Chapter 4

Modeling and Analysis

Local variations in the collected current appear as ‘structure’ on a 2D spatial mapping of the photocurrent. While this directly gives the general uniformity of collection in the material, a more quantitative and precise description of the losses may be desired. As it is not possible to distinguish between the various loss mechanisms with the data at zero bias alone, the photocurrent can be measured as a function of cell voltage. It will be shown in this chapter that fitting of the resulting data with curves generated by simulation of an equivalent circuit allows one to distinguish between various loss mechanisms. Equivalent circuit simulation and examples of data fitting will be presented. Analysis of several complications, including high injection and spot size effects, will also be discussed. Finally, the dependence on wavelength will be examined.

4.1 Equivalent Circuit

Simulation of the equivalent circuit was performed to analyze the apparent quantum efficiency (AQE) versus cell bias data. Equivalent circuit analysis allows evaluation of the effects of resistance and diode parameters on the circuit response. Another option for evaluation of the AQE versus bias data is an analysis of the actual carrier dynamics. Such a treatment would need to include grain boundaries, as well as a description of the device in terms of its electric field and carrier dynamics. This type of analysis could in principle lead to indirect evaluation of carrier parameters such as the minority carrier lifetime and grain boundary surface recombination velocity. However, complications due to the relative size of the laser spot to the grains, the lack of knowledge of basic material parameters, and the existence of extensive defect levels make this type of analysis beyond the scope of this thesis.

The equivalent circuit used for analysis is shown in Figure 4.1, which divides the cell into a large dark area and a small illuminated area. The circuit includes the input resistance of the measurement circuit (R_{in}), as well as resistances associated with the absorber layer and back contact (R_{Lbc} and R_{Dbc}), the CdS/TCO layers (R_{Ltco} and R_{Dtco}), and shunt paths (R_{Ls} and R_{Ds}) of the light (L) and dark (D) parts of the cell. The light source consists of an AC sine wave current source with a DC offset, both chosen to agree with the experimental conditions at each incident laser intensity.

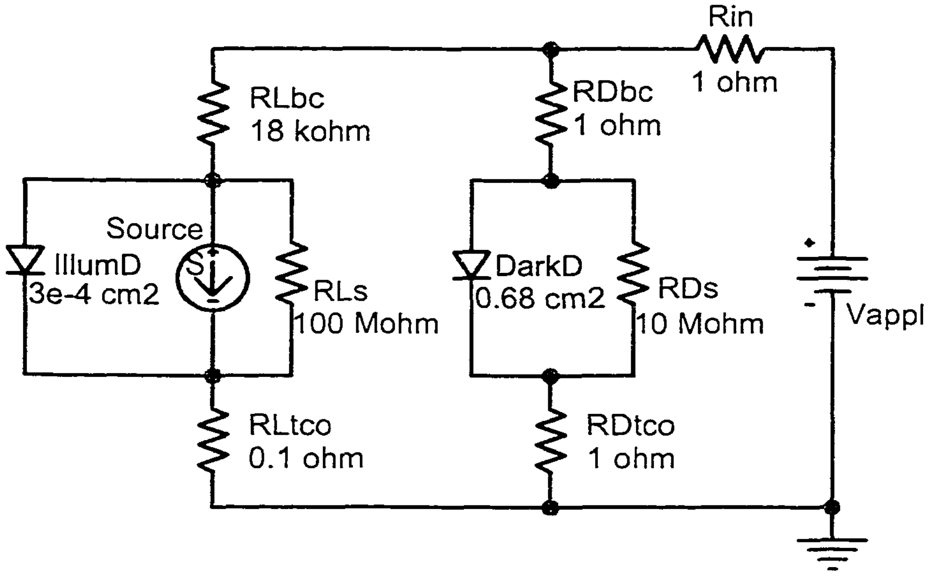

Figure 4.1. Equivalent circuit used for modeling. Note voltage convention that the back contact to the p-type absorber is positive.

Experimentally measured dark and illuminated current-voltage curves were used to determine the model parameters for the diodes labeled DarkD and IllumD, respectively. The use of different model parameters was necessary because of differences in current-voltage curves between light and dark conditions, which is typical of CdTe- and CIGS-based devices.

4.2 Simulation Procedure

Use of a software package (PSpice) to simulate the circuit is preferred over an analytical treatment primarily because of the nonlinearity of the diode equation and the need for a time-dependent solution. The nonlinear nature of the diode and the relatively large magnitude of the source current do not allow the small-signal analysis procedure often used in Pspice simulations to model the behavior of the circuit properly, since the amplitude of the source AC current is large enough to perturb the system beyond the bias point initially calculated by the program. Instead, a time-transient analysis was chosen, which calculates the time-dependent current at R_{in}. This leads to, for example, correct modeling of the forward current of the illuminated diode as the voltage drop due to the photocurrent forces the diode into forward bias. A Fourier transform extracts the AC component of the resulting signal.

4.3 Modeling Results

4.3.1 Induced Voltage

Figure 4.2 shows the local voltage induced across the illuminated diode as a function of time for two spot sizes and applied voltages of 0.0, 0.25, 0.50, and 0.75 V. The parameters used to generate the curves were R_{Lbc} = 20 kΩ, 900 kΩ; A_L = 2.4, 4.4; I_{Ls} = 4.3e-8 A, 2e-5 A; for spot sizes of 100 and 1 μm respectively, where A_L and I_{Ls} are the diode quality factor and saturation current of the illuminated diode (see Section 4.4 for an explanation of the choice of these parameters). The local voltage induced by the photocurrent through R_{Lbc} is noticeable for the 100 μm spot, and very large for the extreme case of a 1 μm spot with the same photocurrent.

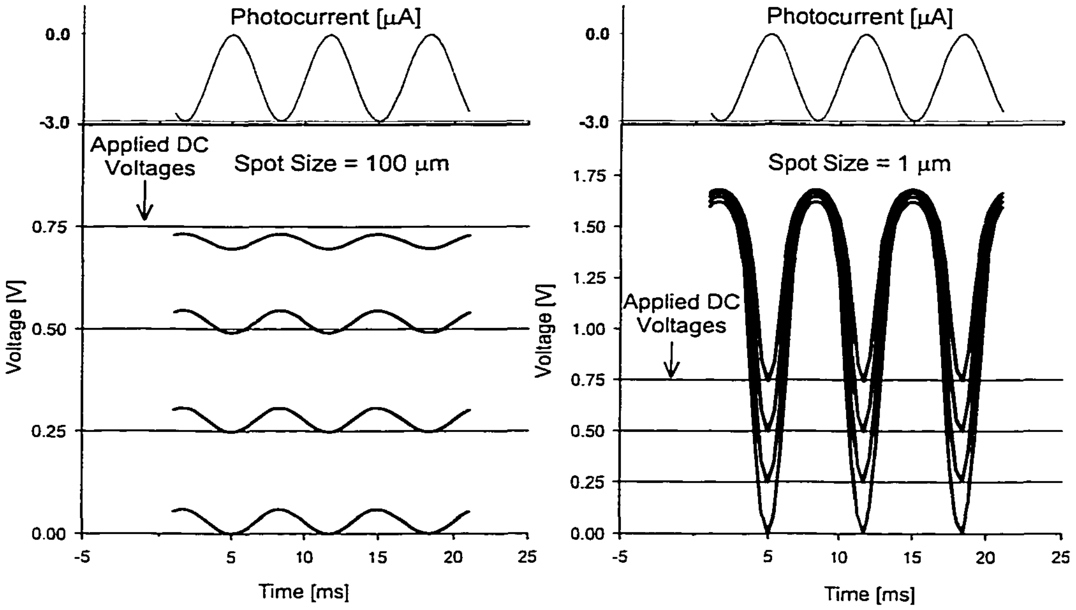

Figure 4.2. Modeled voltage across illuminated diode versus time, at various DC applied biases, for two spot sizes. The photocurrent driving the voltage is also shown for reference.

Figure 4.2 helps explain how the circuit response is affected by R_{Lbc} and the photocurrent. For a low applied voltage, the photocurrent forces the illuminated diode to a larger forward bias than that applied. When the photocurrent drops to zero, the illuminated diode voltage returns to the applied voltage. For high applied voltages, however, the forward current of the diode results in a voltage which opposes that induced by the photocurrent, and the illuminated diode voltage is actually less than the applied voltage. This is applicable to both the DC and AC parts of the voltage. In the case of the 1 μm spot, the voltage induced by the photocurrent is large enough (due to the very large value of R_{Lbc}) to force the diode into far-forward bias, even with zero applied voltage. The saturation-like behavior near 1.5

V is due to the large modulated forward current induced by the forward voltage, resulting from the modulated photocurrent.

That the voltage across the illuminated diode is modulated leads to a fairly simple explanation for the typical drop-off in collected current in forward bias shown in Figure 4.3. The modulated voltage leads to a modulated forward current produced by the illuminated diode (dotted lines). The collected current is then simply the difference between the photocurrent and the forward current. The dark portion of the solar cell does not appear to significantly affect the localized collection in this case.

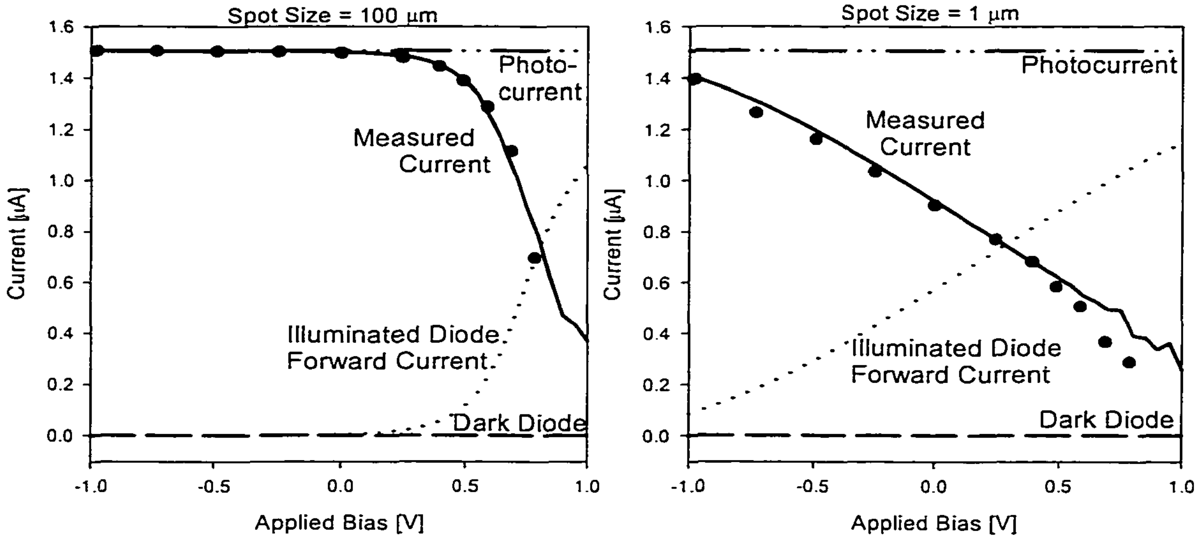

Figure 4.3. Light-induced photocurrent, modeled collected current, and modeled current through the light and dark diodes in the equivalent circuit for two spot sizes. Experimental data shown for reference.

4.3.2 Lateral Size of Induced Voltage Region

The case where the induced voltage is nearly 1.5 V suggests that complications may exist due to a lateral (in the plane of the junction) potential gradient between the illuminated diode and the dark diode. Analysis of this problem could proceed with a distributed model of several dark diodes in parallel with the illuminated diode, connected by resistances representing the lateral conductivity of the layers. With appropriate choices of diode areas and resistances, one could model the fact that nearby dark diodes may be forward biased by an amount proportional to their distance from the illuminated diode. However, since to first order this will have only the effect of increasing the forward current resulting from the voltage induced by the photocurrent, one could also calculate an *effective* area of illumination and compare to the actual spot size.

To evaluate whether the actual and effective spot sizes are significantly different, some simple calculations can be made. Assuming a single layer of thickness t conducts the current (with resistivity ρ), a straightforward analysis shows the resistance from the illuminated diode to a distance r from the edge of the illuminated diode is given by

$$R(r) = \frac{\rho}{2\pi t} \ln\left(\frac{r}{r_1}\right) \simeq 0.8 \ln\left(\frac{r}{r_1}\right) \Omega \tag{4.1}$$

where r_1 is the radius of the illuminated diode. This resistance is in series with the effective resistance of the illuminated diode, forming a voltage divider. In the case of the transparent conducting oxide (TCO) layer, $\rho \approx 2 \times 10^{-4}\,\Omega\,\mathrm{cm}$, and $t \approx 4000\,\text{Å}$ [31] and hence the lateral resistance is the order of 1-10 Ω. The effective resistance of the illuminated diode in forward bias is the order of 2 $\Omega\,\mathrm{cm}^2$ (given by the slope of the current-voltage curve in forward bias). For the spot sizes used in this experiment, this yields resistances above 1 MΩ. Essentially all of the induced voltage drop thus exists across the illuminated diode, and the TCO resistance is small enough to not allow any significant voltage biasing of nearby areas.

Since the back contact is made to a metal with lower resistivity than the TCO layer, the potential drop across the back contact is expected to be less than that across the TCO. The remaining region is within the CdTe or CIGS absorber itself, where of course a potential gradient will be present perpendicular to the junction, due to the ohmic losses through the relatively poorly conducting absorber material. The question is whether the potential spreads laterally. The resistance between grains is typically at least 3 orders of magnitude higher than the bulk resistance in single grains [32], so that the current crossing grain boundaries should be negligible. Since the grains in CdTe and CIGS are generally columnar from the back contact to the CdS layer, the conclusion is that no significant voltage will be generated laterally to the illumination area.

The effective area of illumination is thus expected to be unchanged by current flow to a very good approximation, as long as the grains are columnar and the resistivity of the top and back contacts is low. An exception to this statement may occur when the spot size is smaller than the grain size. This situation may lead to an effective spot size larger than that expected, due to spreading of the current flow over the entire grain.

4.3.3 Variation of Photocurrent with Bias

Once reasonable parameters for the light and dark current-voltage curves are generated, fitting of data must be performed by varying a subset of the diode parameters and/or the resistive components in the equivalent circuit. Figure 4.4 shows the effects of changing major parameters on the shape of the AQE versus bias curve. The base curve, which already includes some resistive loss, corresponds to a typical good fit to data taken with a 5 μm spot with high laser intensity. The data is plotted in terms of 'Circuit AQE', which is simply the percent of the internal photocurrent which is collected externally.

A shunt path (squares in Figure 4.4), results in a vertical overall shift in the AQE curve, in contrast to the increased slope at zero bias resulting from shunting effects in a current-

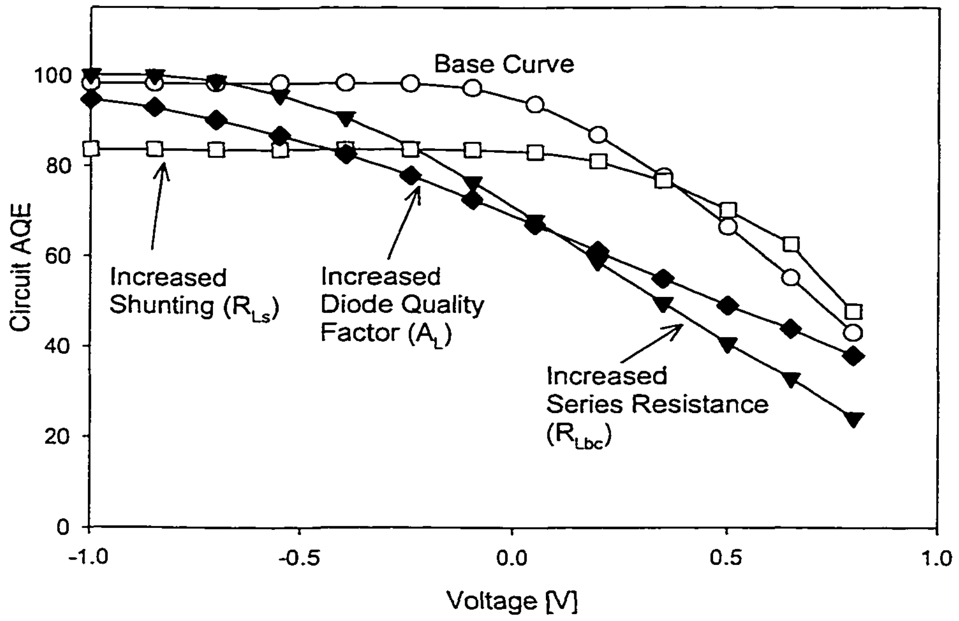

Figure 4.4. Modeled data showing the effect of various parameters on the resulting curves.

voltage curve. The other possible major effects presented are a shift in the curve to lower voltage for increased series resistance, and a reduced forward bias slope due to an increase in the diode quality factor.

4.3.4 Local Diode Variations

It is important to note that the previous analysis is valid so long as the local diode characteristics are similar to the whole-cell characteristics. This will not always be a valid assumption. In particular, the forward current may vary considerably from one position to another, which will complicate matters considerably, since the magnitude of the AQE dropoff in forward bias, as well as the bias at which it the dropoff begins, will be directly affected by an locally increased forward current. Hence spatial variations in the forward current may be difficult to separate from variations in the series resistivity.

4.4 High Injection Effects

4.4.1 Effect on Diode Characteristics

As the laser intensity is increased (due to higher laser power or the use of a more finely focused spot), the illuminated diode can be forced into the high injection mode. That is, the photo-generated minority (electron) density will be higher than the majority (hole) doping concentration. This will result in two main effects. The first is that ohmic losses will be significant, which is accounted for in the modeling with the resistor R_{Lbc}. The second is that the minority carrier dynamics will be affected, due to carrier inversion. A first order effect of high injection is an effective increase in the diode quality factor of the illuminated diode due to the relation:

$$np \leq n_i^2 \exp\left(\frac{qV_a}{k_b T}\right) \tag{4.2}$$

where n, p are the electron, hole concentrations, n_i is the intrinsic carrier concentration, V_a is the applied voltage, k_b is Boltzman's constant, q is the electronic charge, and T is the temperature. This relationship exists because the separation of the quasi-fermi levels must be less than the applied voltage, due to the ohmic voltage drop [11, pg. 93]. When $n \sim p$, the dependence of minority carrier concentration on voltage contains an extra factor of $\frac{1}{2}$ in the exponential, which corresponds to an increase in the effective diode quality factor by 2, since the voltage dependence of the forward current follows from the voltage dependence of the carrier population [12].

For this reason, when fitting data taken at high injection, the diode quality factor of the illuminated diode is roughly increased by two. This is a first order correction where other effects due to changes in minority carrier dynamics are expected to play a role. More reasonable fits can be obtained to the data in this way. It must also be noted that the open circuit voltage of the diode is kept constant by reducing the saturation current of the diode. This is done because the diode quality factor and the saturation current are not independent parameters.

4.4.2 Calculation of Injected Electron Concentration

The injected (electron) carrier density is given by:

$$n(z) = \frac{P\tau}{\alpha}\frac{\lambda}{hc}e^{-z/\alpha} \tag{4.3}$$

where P is the incident power density, τ is the minority carrier lifetime, α is the penetration depth, and z is the distance into the absorber.

The hole concentration in CdTe, derived from capacitance-voltage measurements, is ~2×10^{14} cm^{-3}, and for a (reasonable) lifetime of 10^{-8} s, a penetration depth of 0.25 μm [7], and for the experimental conditions used, Figure 4.5 shows that high injection is expected to occur at least near the surface of the CdTe absorber at an incident power density of 300 mW / cm^2, or just a few suns. The onset will of course occur at a higher power density for CIGS and other types of solar cells in this study, due primarily to higher absorber majority doping concentrations.

4.5 Spot Size Dependence

The main reason for taking measurements at multiple spot sizes is that it is necessary to use a large spot when mapping a large area in a reasonable amount of time. A large spot samples a greater fraction of the area under study, so that fewer data points need be taken. The resolution is given approximately by the e^{-2} half width of the beam. Changing the spot

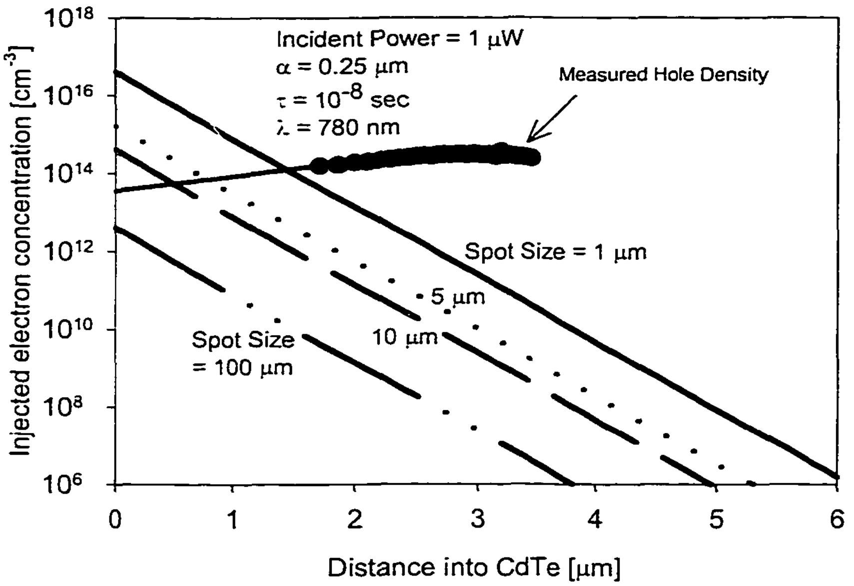

Figure 4.5. Calculation of injected carrier density for CdTe. Slopes based on assumed penetration depth, or inverse absorption coefficient, of 0.25 μm.

size will affect both the incident power density and the area over which the photocurrent flows. Adjustment of the laser attenuation to keep the incident power density consistent will then change only the area of current flow. Fitting AQE versus bias data taken with multiple spot sizes will then result in a series of resistances for the best fit, and should yield a single resistivity, assuming the current flow is cylindrical, with a cross-sectional area given by the illumination area.

The nonlinearity of the diode curve forces care to be taken to keep the power density very consistent when data is taken with different spot sizes. As shown in Figure 4.2, a small incident power density (graph on left) will only vary the bias in a small range near the applied bias, whereas a large incident power density (graph on right) will 'sample' much more of the diode curve even with zero applied bias. The two cases could in principle be compared if one had confidence in the extrapolation of the diode curve to far-forward bias. However, data is typically not taken so far into forward bias, as the high currents resulting

Table 4.2. Penetration depths of lasers used in experiment.

Room Temperature Wavelength (nm)	CdTe α^{-1} (μm)	CIGS α^{-1} (μm)
638	0.215	0.165
685	0.261	0.193
788	0.474	0.289
823	1.43	0.345
855	34.6	0.405

from an entire cell in forward bias may heat the illuminated regions or otherwise cause damage to the cell. For evaluation of the series resistivity of the material, it is recommended to duplicate conditions as much as possible, varying only the spot size.

4.6 Dependence on Wavelength

4.6.1 Generation Volume

The penetration depth of photons given in Figure 2.3 shows that the generation volume of minority carriers will depend on wavelength. Table 4.2 shows the penetration depths (the inverse of the absorption coefficient α) for each room temperature laser wavelength, for both CdTe (E_g = 1.48 eV) and CIGS (E_g = 1.11eV) absorbers [8]. Note that due to differences in fabrication, the actual penetration depths may vary somewhat among devices. These values do show that changes in the generation volume can be affected by changing the laser wavelength. The generation volume directly controls the density and position of injected electrons relative to the junction. In this way the transition to the high-injection regime can in principle be controlled by wavelength. However, this effect is expected to be difficult to separate from the collection dependence on distance from the junction that the carrier is generated. When a carrier is generated further than one diffusion length from the edge of the depletion region, the likelihood of that carrier recombining is in general greater, resulting in a falloff in collection.

4.6.2 Local Bandgap Variation

As shown in Figure 4.6, devices manufactured by different methods have very different responses near the band-edge of CdTe. This has been investigated in some detail using photoluminescence [33–35], but has never before to the author's knowledge been investigated with a high spatial resolution measurement of the wavelength-dependent photocurrent. Bandgap variations have generally been attributed to sulfur alloying of CdTe near the junction. CdTe has a nominal bandgap of ~1.5 eV, and CdS of around 2.4 eV. However, the $CdTe_{1-x}S_x$ system exhibits band-bowing; small amounts of S in CdTe will decrease the bandgap of the material, as shown in Figure 4.7 [36]. Regions of reduced bandgap

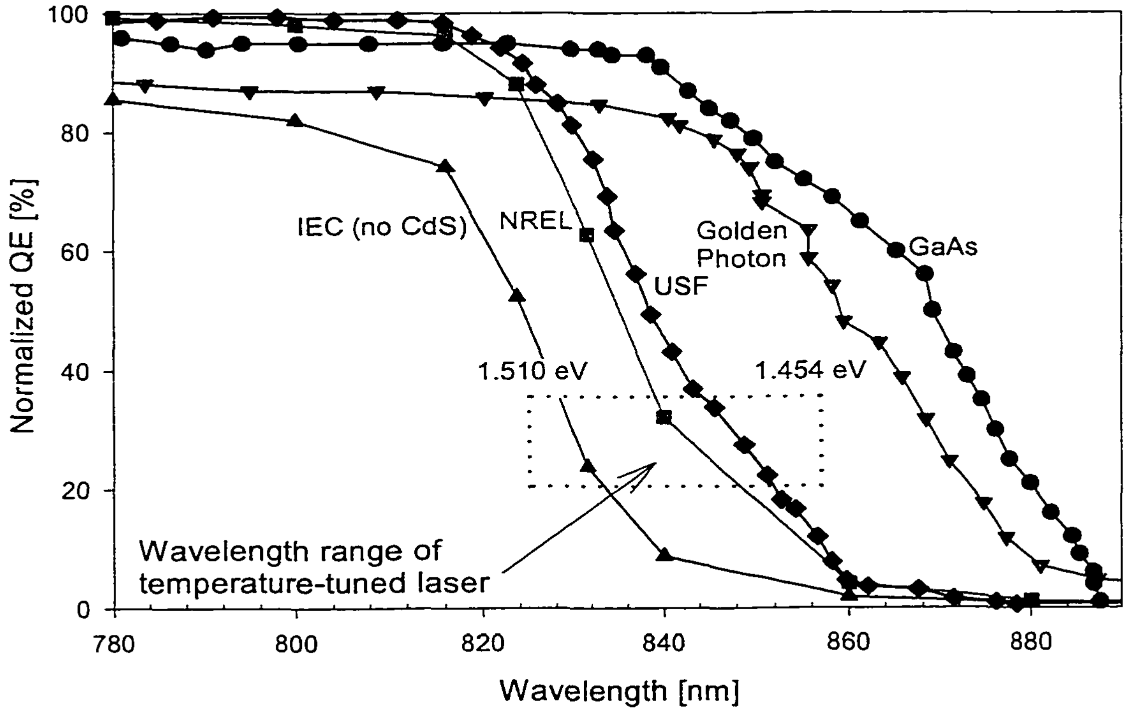

Figure 4.6. Quantum efficiency near the band-edge of CdTe for selected devices, showing wavelengths accessible with temperature-tuned laser.

will absorb photons with energies below the pure-CdTe bandgap. Typical reductions in the bandgap range from 10 to 65 meV, and the temperature-tuned laser can cover ~50 meV of the range. This energy range (from 1.50 to 1.45 meV) corresponds to sulfur incorporations from $x = 0$ to $x = 0.045$ [36].

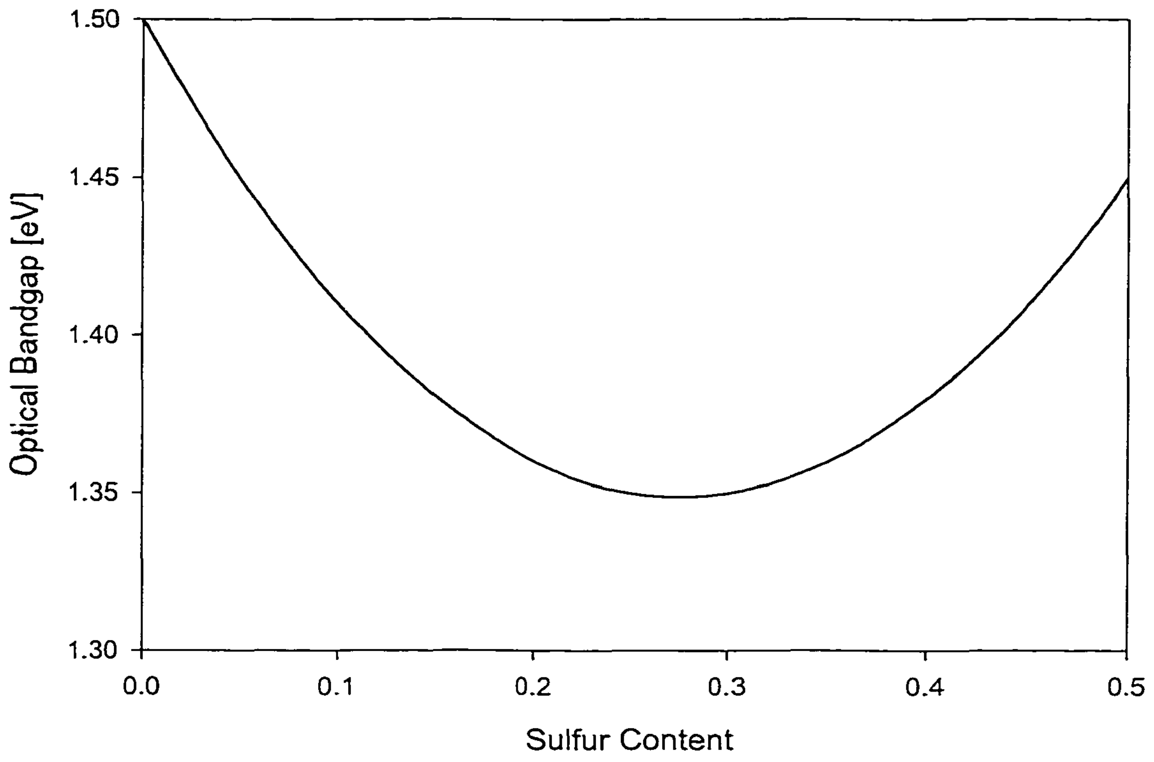

Figure 4.7. Illustration of band bowing due to Sulfur incorporation in CdTe.

Since high spatial resolution photoluminescence measurements have found changes in the energy of luminescence (corresponding to changes in the bandgap) between the center of grains and the grain boundary itself, it is expected that local spatial variation in the bandgap will be observed. This phenomenon has been attributed to the fact that the diffusivity of sulfur is higher down grain boundaries than through the bulk of the material [35]. Mapping of the photocurrent over an area with multiple wavelengths will be shown to clearly exhibit absorption of sub-bandgap photons in localized regions (and collection of the resulting photocurrent).

4.7 Temperature Rise Induced by the Laser Beam

The question of the local temperature of the illuminated diode, if extrapolated from common knowledge about the temperature rise of whole devices under illumination, is potentially critical. Solar cells under 1 sun illumination show increases in temperature the order of 20 °C. The highest intensities used in this experiment are several thousand suns equivalent. However, the geometry is quite different in the case of a localized spot of illumination, and the literature shows an upper limit to the temperature rise induced, for the geometry of a thin slab of material of thermal conductivity K, is given by

$$T_{rise}^{\max} = \frac{P}{2\pi^{\frac{1}{2}}Kr} \tag{4.4}$$

where P is the integrated incident intensity and r is again the radius of the incident spot [37]. This analysis is applicable to solar cell devices, and the calculated maximum rise is the order of 0.1 °C, given a thermal conductivity for CdTe the order of 50×10^{-3} W °C / cm [38], and an incident power of 1 μW at the 1 μm spot size (1000 suns). Even if the thermal conductivity were lower by an order of magnitude due to the presence of grain boundaries, the actual temperature rise due to absorption of the laser illumination will not be enough to perturb the diode characteristics significantly, since the parameter most sensitive to temperature, the open circuit voltage, typically varies by only -2.0 mV / °C.

Chapter 5

Observed Spatial Variations in Solar Cell Collection

Variations in spatial uniformity of polycrystalline solar cells, in particular CdTe and CIGS cells, are examined in terms of photocurrent collection over the cell area. The analysis of Chapter 4 will be used to show that regions of non-uniform collection in these types of cells can be attributed to various causes, including resistive, high injection, and bandgap variation effects. The degree of variation will be shown to be dependent both on the cell type and specific processes, as well as post-deposition treatments. The variations exhibited by three types of solar cells (polycrystalline CdTe and CIGS, and crystalline GaAs) will be contrasted. Resistive and bandgap variation effects will be examined, and their presence in CdTe cells manufactured by two processes will be contrasted. A post-deposition $CdCl_2$ treatment will be shown to strongly influence the number of variations seen in CdTe cells. Finally, non-uniformities induced by light and heat stress on the sample will be shown on a CdTe cell.

5.1 Overall Uniformity Comparison

The extent to which the whole-cell performance is affected by non-uniformities can be evaluated with this technique, at least in terms of the uniformity of the current collection. One possibility is that large portions of the solar cell have a lower response to incident illumination, leading to an overall low efficiency. Another is that defect areas small compared to the cell area have only a minor effect on the total photocurrent, but significantly affect the cell in other ways. The latter will be shown to be much more common in all cells studied with this technique.

The standard representation adopted here to designate how much a cell is affected by non-uniformities is a map of the apparent quantum efficiency (AQE) over a significant portion of the cell. For reference, a representative sample is shown in Figs. 5.1, 5.2, and 5.3 for three types of solar cells: CdTe, CIGS, and GaAs. The cells chosen are all high quality solar cells, resulting from laboratory scale deposition processes. The results shown are meant to evaluate the impact of non-uniformities on the overall efficiency of the best cells being produced today in the laboratory.

All three graphs in Figure 5.1 show data taken with "low resolution" (100 μm spot size) at ~0.2 suns laser illumination, with the 638 nm laser. The device in each case is held at zero bias, so that the laser is probing the local quantum efficiency near short-circuit conditions. The top portion of each shows a contour plot of the data; on the x-y plane is the projection of the data. In each case a corner of the cell is shown. The contrast scale is identical in each case; the data below 50% response (35% for GaAs) has been hidden for presentation purposes. The CIGS and GaAs cells have grids which are responsible for the linear features. The large reduction in response on the GaAs cell near $Y = 3200$ μm is due to an visible spot of metal on the surface.

With this set of conditions, only the CdTe cell shows a defect, along with a slight reduction in collection near the corner of the cell. The average response of the GaAs is reduced by grid coverage, since the spot size is large enough to have part of the beam incident on a grid at all times. The lack of an anti-reflection coating also results in a lower measured quantum efficiency. These graphs show that the cells are largely uniform over the

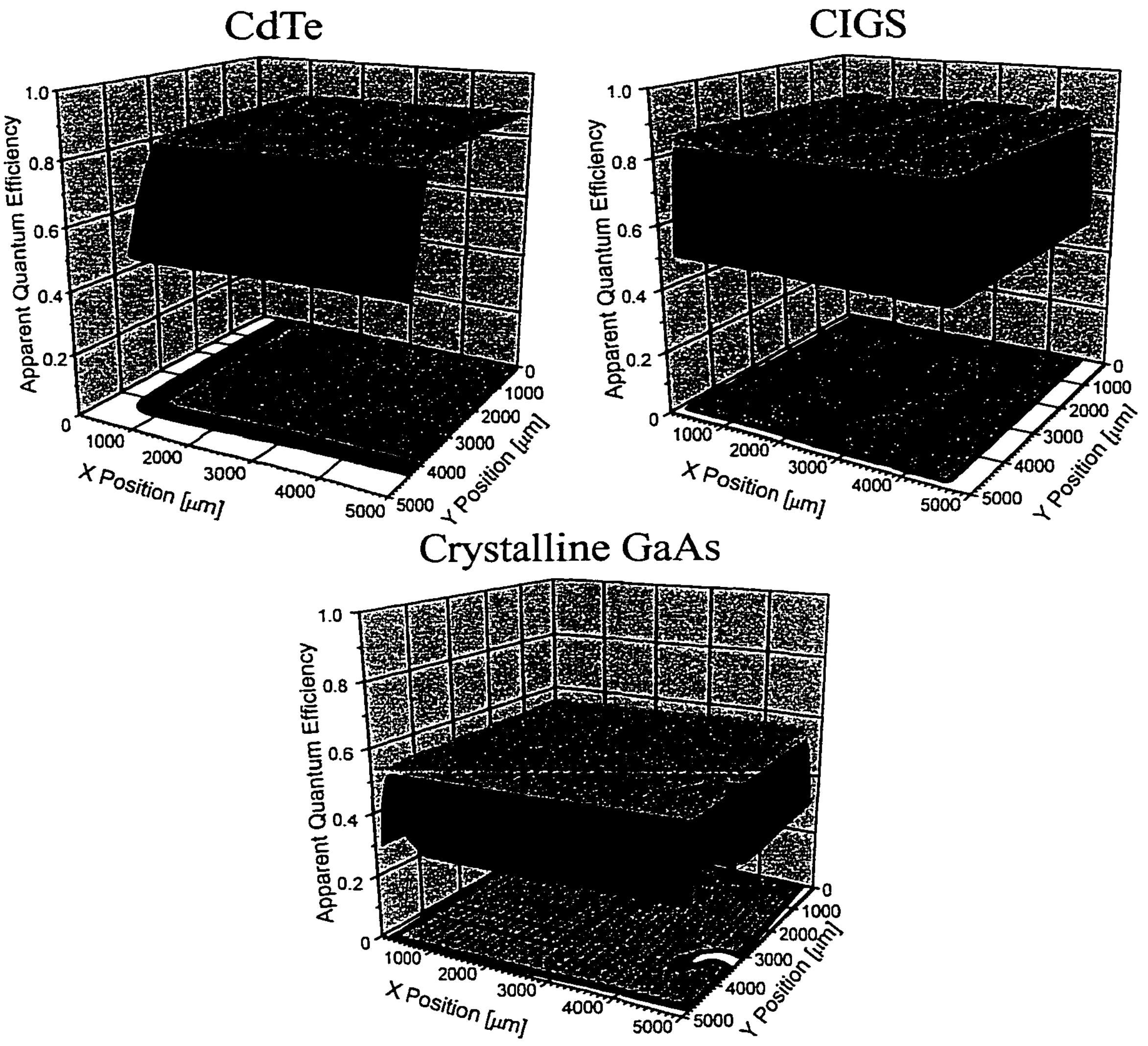

CdTe

CIGS

Crystalline GaAs

Figure 5.1. Spatially dependent quantum efficiency on three types of solar cells. Low resolution, 100 micron spot, 0.2 suns equivalent laser illumination used in each case, with the cell held at zero bias.

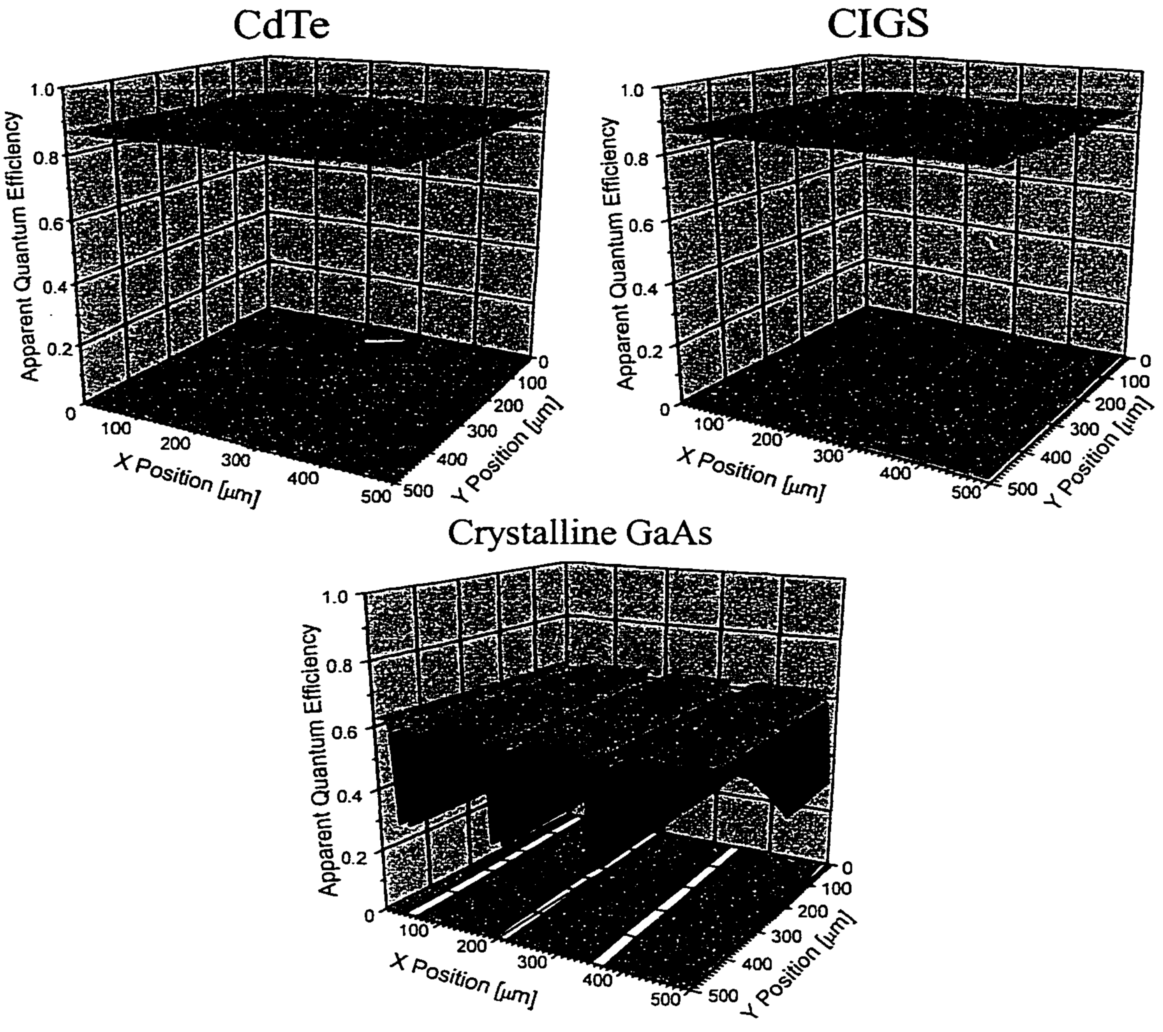

Figure 5.2. Medium resolution data for three types of solar cells. 10 micron spot, 1 sun equivalent laser illumination used in each case, with the cell held at zero bias.

device active area, lacking any large gradations in collection performance across the cell. These examples are typical in this respect for all cells studied with the apparatus to date.

Higher resolution mapping of the quantum efficiency verifies that CdTe cells show the greatest number of non-uniformites among the cells studied under the test conditions. Figure 5.2 shows data taken on the regions shown as squares in Figure 5.1, with a 10 μm spot size ("medium resolution") and 1 sun laser illumination. The graphs again show fairly similar uniformity, the maximum GaAs quantum efficiency is higher in this case since the spot is not obscured by the grids.

When the highest resolution is used at low intensity (1 μm spot, 1 sun illumination), local regions of reduced collection are apparent in both the CdTe and CIGS cells, while the GaAs cell shows extremely uniform collection over the 50×50 μm area. Figure 5.3, which shows data taken over the area in the squares in Figure 5.2, shows reductions in quantum efficiency over regions 5-10 μm in size. It should be noted here, however, that further investigations show that the cause of the lower response differs between the CdTe and CIGS cells used in Figure 5.3. The spot of lower collection on the CdTe cell shows bias and intensity dependence, while the 'defects' on the CIGS cell do not. This indicates that regions of lower response for the CIGS cell are due to local optical defects (most likely spots of metallization resulting from the grid application process), while the 'defects' on the CdTe cell are electrical in nature. This is significant in that optical defects to first order merely reduce the short-circuit current, while electrical defects can affect the diode curve of the entire cell.

While there apparently do exist cells with very uniform collection over the entire cell active area, examples also exist of cells where spatially dependent collection is very pronounced, even in reasonably efficiency cells. Figure 5.4 shows data taken at low, medium, and high resolution on a 10% efficient cell produced at the Colorado State University Materials Engineering Laboratory. The circular outline of the cell can be seen in the low resolution data. Higher resolution data is again taken on the areas shown as the square in the graph of the next lower resolution data. The data was taken under conditions identical to those in previous cases, with the exception of the graph on the bottom of the figure, which

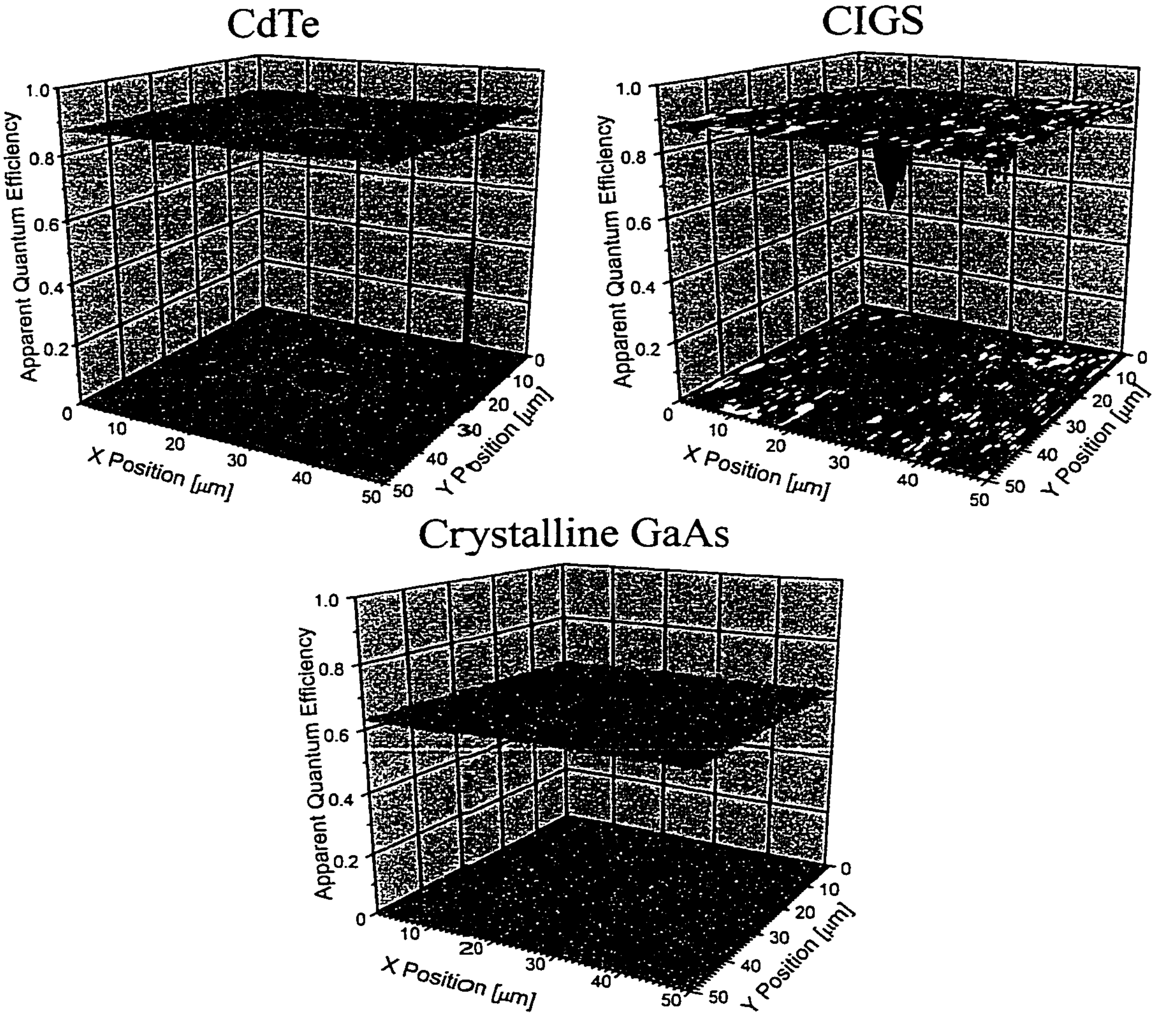

Figure 5.3. High resolution data for three types of solar cells. 1 micron spot, 1 sun equivalent laser illumination used in each case.

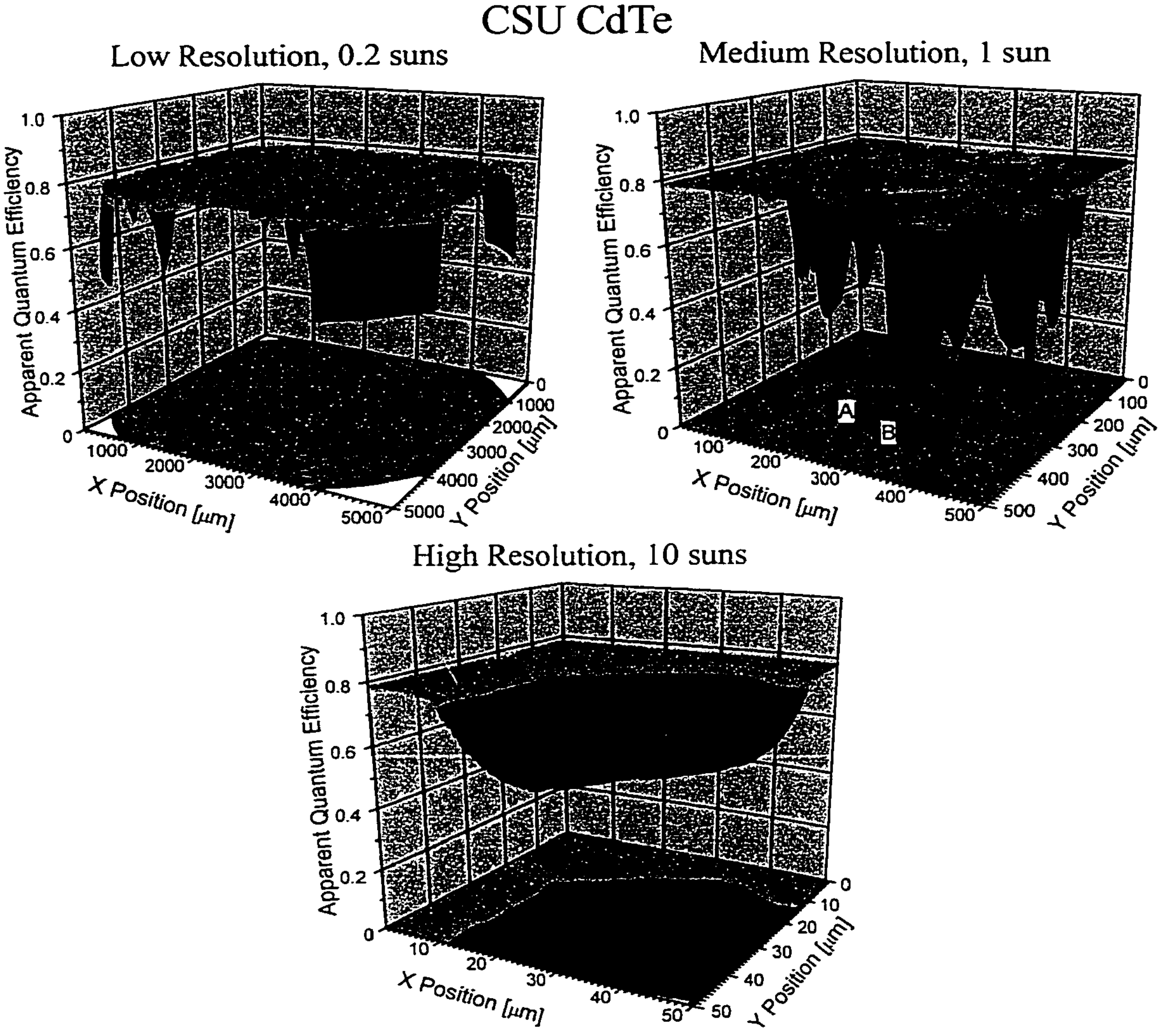

Figure 5.4. Spatially dependent quantum efficiency for low (top left, 0.2 suns), medium (top right, 1 sun), and high (bottom, 10 suns) resolutions.

is taken with 10 suns equivalent laser illumination. This cell clearly shows a large number of local reductions in the collection.

5.2 Resistive Effects

Typically, large area scans such as those shown in Figure 5.1 are used to identify positions of reduced collection, but apart from obvious features such as grids and cell edges, the cause of the reduction is not usually apparent. As has been shown in this thesis, the intensity and bias dependence of the response can be used to distinguish electrical from optical defects, and modeling can be employed to yield more specific information about the cause of the lowered response.

Figure 5.5 shows the bias dependent AQE with the spot centered on two positions, which are labeled on the upper-right graph of Figure 5.4. The top graph shows that intensity variations in AQE taken with the spot centered on the position labeled 'A' are minimal; whereas those taken with the spot centered on the defect (labeled 'B') are very substantially affected. The bias and intensity dependence in Figure 5.5 clearly indicates that the defect is electrical in nature. Furthermore it can be reasonably well modeled with the equivalent circuit.

Figure 5.6 shows equivalent circuit modeling results for the set of data taken on position 'B'. The best fit curves were generated by varying the series resistance R_{Lbc}; shunting effects were also included for the 100 μm spot size. The curves indicate that the reduction in collection is primarily due to series resistance effects, with shunting effects playing a secondary role. The 1 μm spot at point A, incidentally, is fit with $R_{Lbc} \simeq 2$ MΩ, about a factor of 10 lower than at point B.

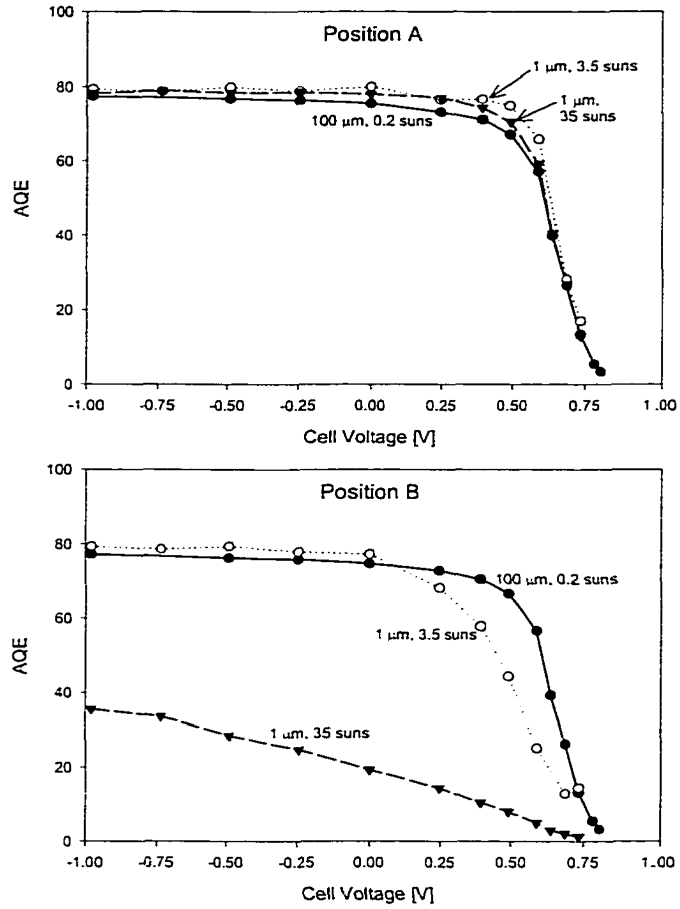

Figure 5.5. AQE versus bias for two positions, with various spot sizes and intensities.

5.3 Intensity Effects

Modeling predicts that the photocurrent collection should be independent of spot size as long as the incident power density is kept constant, assuming the material is isotropic over the spot sizes considered. However, Figure 5.7 clearly shows an example where this is not the case. The intensity dependence at the same positions as in Figure 5.5 is shown for three spot sizes. While, as expected, the reduction starts at higher incident power for larger spot sizes, at neither position is the power *density* at which the reduction begins consistent among spot sizes. In fact, the 10 μm spot shows a reduction with about a factor of 10 less

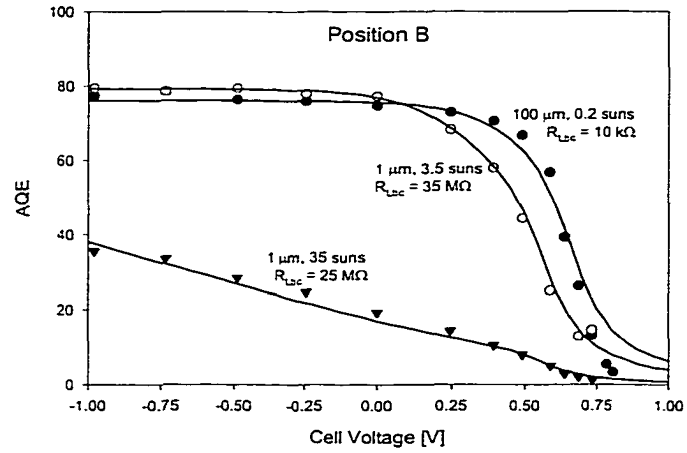

Figure 5.6. Data (symbols) and best fit curves from equivalent circuit modeling (lines). Best fit curves generated by varying only R_{Lbc}.

incident power density than the 1 μm spot. This is true for both positions and in fact to some degree for all CdTe investigated to data with this technique.

Since the 1 μm spot size is of the same order as the grain size, it is possible that the effective area of illumination is increased. This may be due to lateral spreading of the current flow over the entire grain, as stated in Section 4.3.2. Thus a lower effective resistance will result due to the larger effective area, which in turn will increase the power density need to produce a reduction in the collection. This possibility, however, will be complicated by the fact that the current flow over the larger area should result in the bias also being effective over the larger area, which in turn will result in a larger forward current which cancels the photocurrent. For consistency with the intensity dependence of the 10 μm curve, an effective spot size of ~3 μm is implied, consistent with typical CdTe grain sizes.

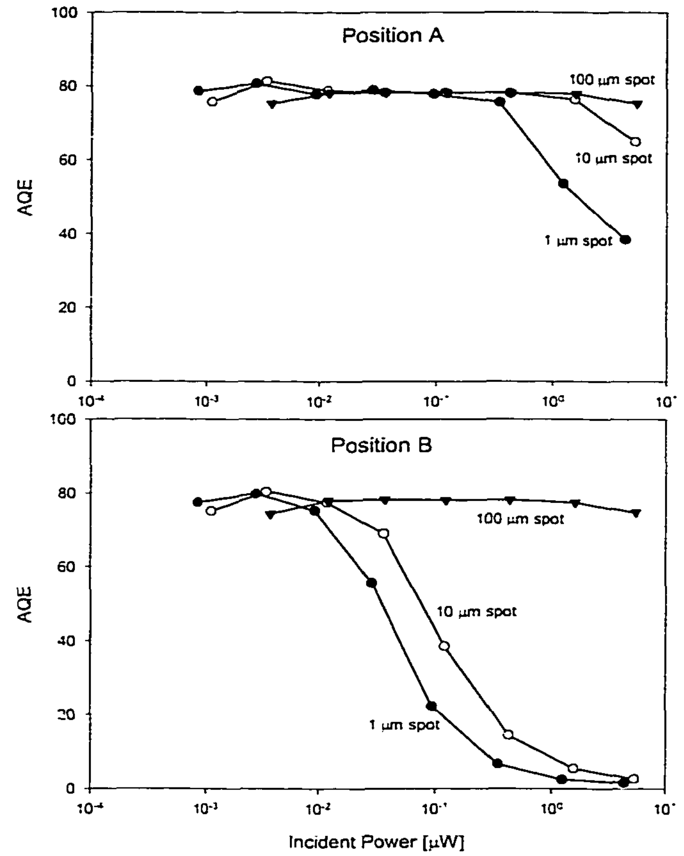

Figure 5.7. AQE intensity dependence for two positions and three spot sizes.

5.4 Bandgap Variations

The application of a laser which is temperature-tuned through photon energies near the bandgap of CdTe has proven to be quite useful. Keep in mind that for pure CdTe, with an optical bandgap of 1.50 eV, very little absorption of photons with lower energies is expected for typical cell absorber thickness. Thus any significant collection efficiency with sub-bandgap photon energies must be due to absorption by semiconductor material with a reduced bandgap, such as the intermixed alloy $CdTe_{1-x}S_x$, or by significant spatial variations in band-tailing or electric field.

The collection of carriers excited far from the junction can be enhanced by a locally strong electric field, since the carriers are more likely to be swept to the junction. Since sub-bandgap energy photons have longer penetration depths, and so are absorbed deep into the material, a local increase in the electric field could enhance their collection. However, the analysis below will show that the regions exhibiting enhanced collection with sub-bandgap energy photons show relatively poor collection with above-bandgap energy photons. If the electric field were indeed higher in these regions, one would expect good response to all wavelengths. Thus it is not likely that the bandgap variations are due to local variations in the electric field.

Band-tailing, where the bandgap is effectively decreased through defect states present near the edges of the valence and/or conduction bands, could also explain the sub-bandgap collection. This possibility cannot be directly discounted using the data in this thesis, although one would generally not expect carriers excited into tail states to be very mobile. However, photoluminescence studies of CdTe in the literature show similar variations in bandgap, as discussed in Section 4.6.2. Further, the researchers find that the dependence on injection density is inconsistent with luminescence through defect states, but that the CdTe cells show band-to-band recombination at energies lower than the CdTe bandgap, clear evidence of a lowered bandgap due to alloying [34]. In fact, the correlation with photoluminescence studies strongly suggest that the observed effect is due to changes in the material bandgap due to sulfur alloying.

Since the reduced bandgap is most likely directly attributable to sulfur alloying, observations of the variations in bandgap effectively probe the uniformity of the CdS-CdTe interface. One might assume that variations in alloying are due to faster sulfur diffusion in

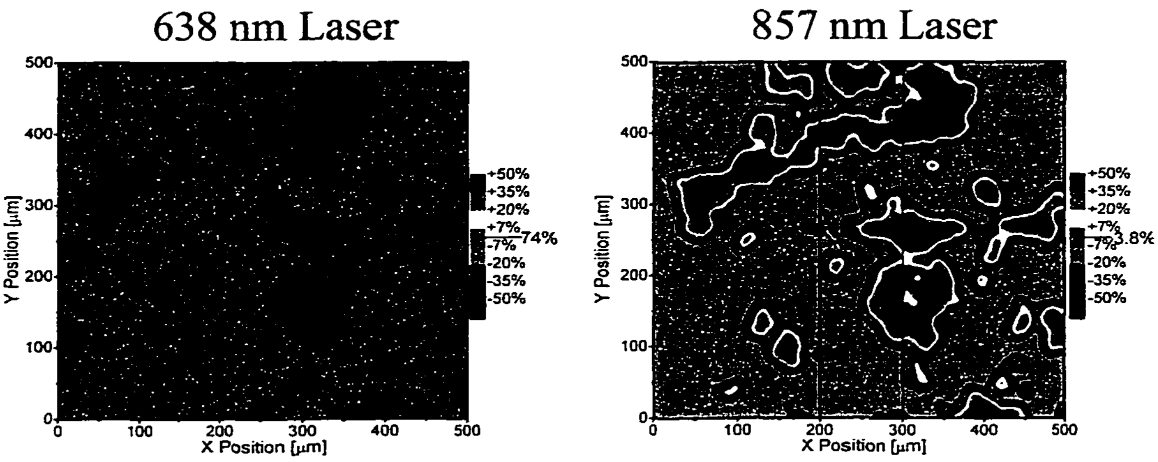

Figure 5.8. Comparison of the AQE versus position with two lasers, one with above-bandgap photon energy (left), the other with sub-CdTe-bandgap photon energy.

some regions. Knowledge of the uniformity of the interface region may be particularly useful, since it is possible that small regions with a poorly formed interface have an influence on the overall device performance.

Figure 5.8 shows identical regions of the cell also shown in Figure 5.4. The data was taken under the same conditions in both cases, with two wavelengths: 638 (left), with photon energy well above the CdTe bandgap, and 857 nm, which has photon energy just below the pure-CdTe bandgap. The very large variation in response with the 857 nm laser is clear evidence for spatial variation in the optical bandgap of the material.

Several observations can be made about this data: 1) The regions of lower bandgap material are in this case large compared to the grain size. 2) Regions of *increased* response due to the lower bandgap correlate very strongly with *reduced* collection when the 638 nm laser is used. 3) The collection is much lower for the 857 nm laser than the 638 nm laser even for the most strongly responding area (6% versus 78%). This suggests that only a small portion of the illuminated material is strongly alloyed, presumably near the interface.

The reduced absorption also results in a lower photocurrent. Since the amount of reduced collection on the defect with the 638 nm laser is dependent on intensity (or effectively the photocurrent), the lower absorption of sub-bandgap energy photons will also lessen the reduction caused by the defect. This consideration complicates the interpretation of the data.

Figure 5.9 demonstrates the wavelength dependence of a portion of the region denoted by the lines in Figure 5.8. The contrast in each case is again consistent with variations from the mean response over the entire area. A clear transition in the data is seen. The data at specific points can also be plotted as the AQE versus wavelength, as shown in Figure 5.10. This data more clearly shows the wavelength dependence of the response for positions on and off of the feature.

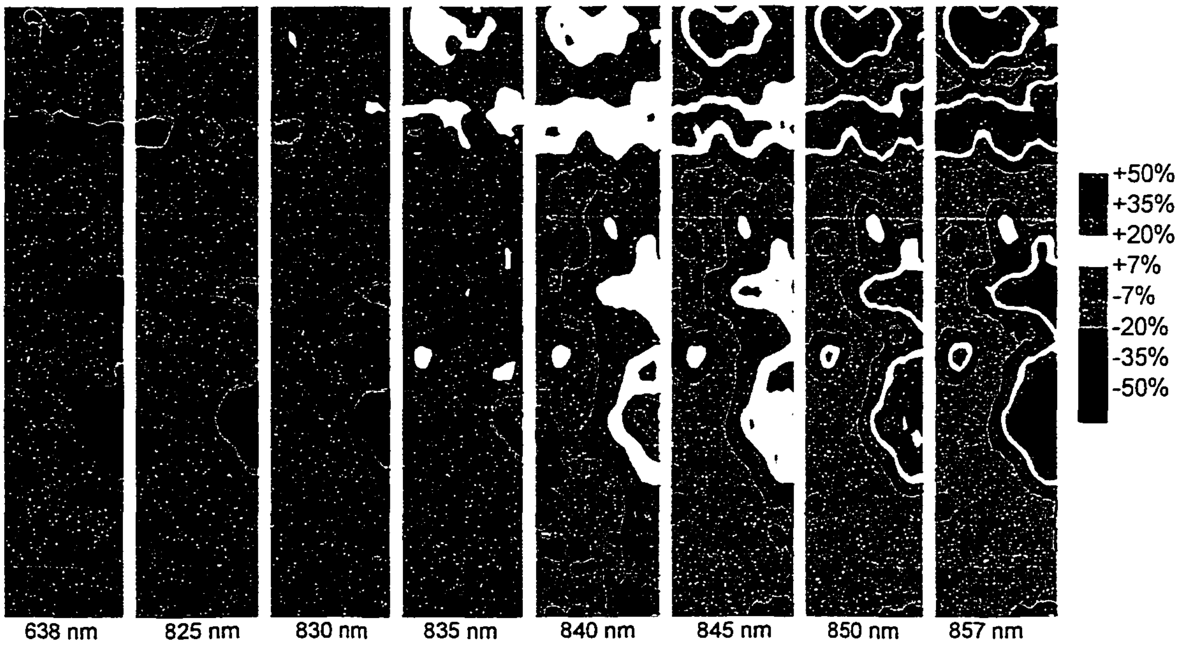

Figure 5.9. Response over a 500 x 100 micron area with multiple wavelengths as labeled. The contrast in each case is consistent with the variation from the mean value. Identical conditions were used for each set of data: 10 micron spot, 1 sun illumination.

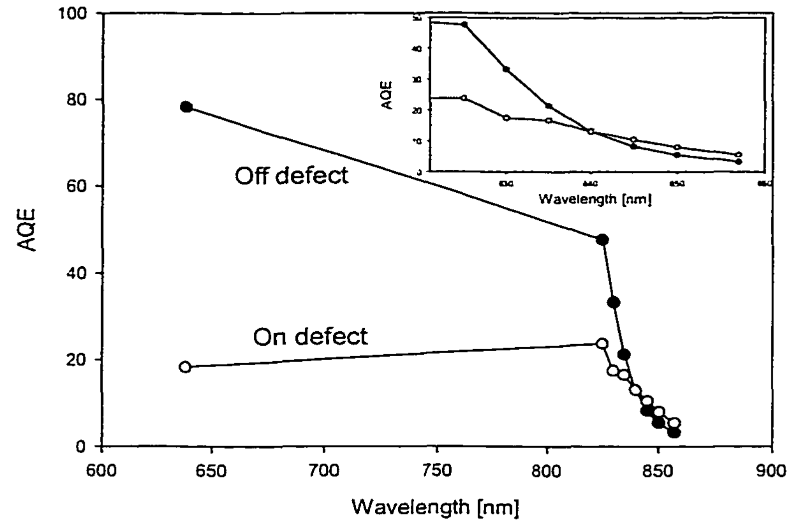

Figure 5.10. AQE versus wavelength for positions centered on and off of a defect. A 10 micron spot with 1 sun illumination was used. Note crossover near AQE of 10%.

The data suggests that an non-uniformly alloyed layer exists at the interface, which could result from non-uniformity of the interface or local enhancement of sulfur diffusion. The correlation between the alloyed regions and the defects suggests that either the more-strongly alloyed region is of poor quality, leading to a high resistivity, or that sulfur diffusion is enhanced where defects are present. Subsequent observations will help to separate these two possibilities.

5.5 Effect of $CdCl_2$ on Cell Uniformity

As shown in Section 5.1, the best-case CdTe solar cells show very few regions of reduced collection under 1 sun equivalent laser illumination. As the post deposition of $CdCl_2$ treatment affects the overall efficiency of the device strongly, a set of samples with and without this treatment were prepared by collaborators at NREL. Note that all other CdTe cells shown in this thesis have been processed with a $CdCl_2$ treatment.

Identically prepared samples, except for the use of a $CdCl_2$ treatment in one case, show dramatically different electrical response. The whole-cell JV and QE curves, shown in Figure 5.11, indicate a increase in short-circuit current, open-circuit voltage, and fill-factor as a consequence of the post-deposition $CdCl_2$ treatment.

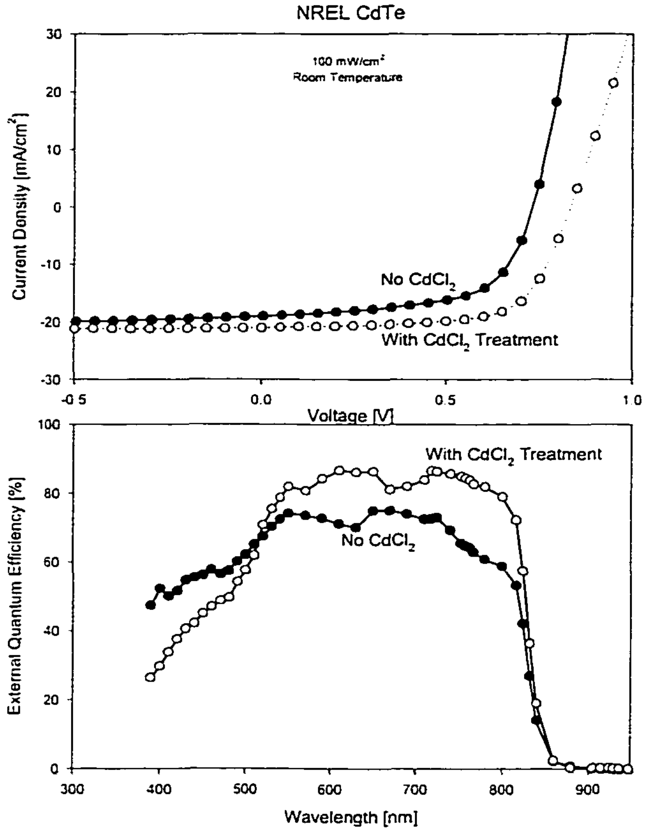

Figure 5.11. Current-Voltage (top) and Quantum Efficiency curves for otherwise identical NREL CdTe cells with and without $CdCl_2$ treatment.

Investigation of the overall uniformity indicates that the $CdCl_2$ treatment does increase the uniformity of collection for above-bandgap photon energies. Figure 5.12 shows the response to sub-bandgap laser wavelengths for a GaAs cell and the CdTe cells with and without the $CdCl_2$ treatment. The contrast is again consistent between all graphs. On this contrast scale, the GaAs response is completely flat over the 50×10 μm area, and the treated CdTe cell shows only a few regions of reduced collection. The untreated CdTe cell, however, shows a great deal of variation in the collection efficiency for photon energies above the bandgap energy.

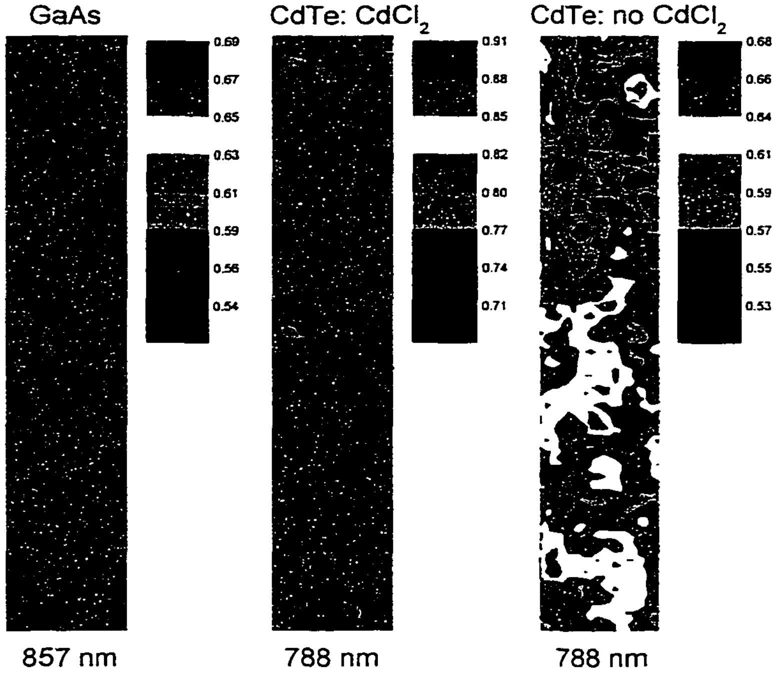

Figure 5.12. Response to above-bandgap photon energies for a GaAs cell, and NREL CdTe cells with and without $CdCl_2$ treatment. A 1 micron spot, with 1 sun incident laser illumination was used for each. Each graph shows a 50×10 micron area.

Another way to present the variation in response is to calculate the maximal variation in the measured photocurrent over a certain area. This is scaled to the mean response over the (in this case) 50×10 μm area and plotted versus photon energy in Figure 5.13. The GaAs cell shows a very small maximal variation for both wavelengths examined. The untreated CdTe cell shows the largest variation for above-bandgap incident photon energy, as is consistent with Figure 5.12. However, the treated cell shows much more variation for photon energies below the pure-CdTe bandgap. This suggests that the $CdCl_2$ treatment is responsible for causing non-uniform diffusion of sulfur into the CdTe layer near the interface.

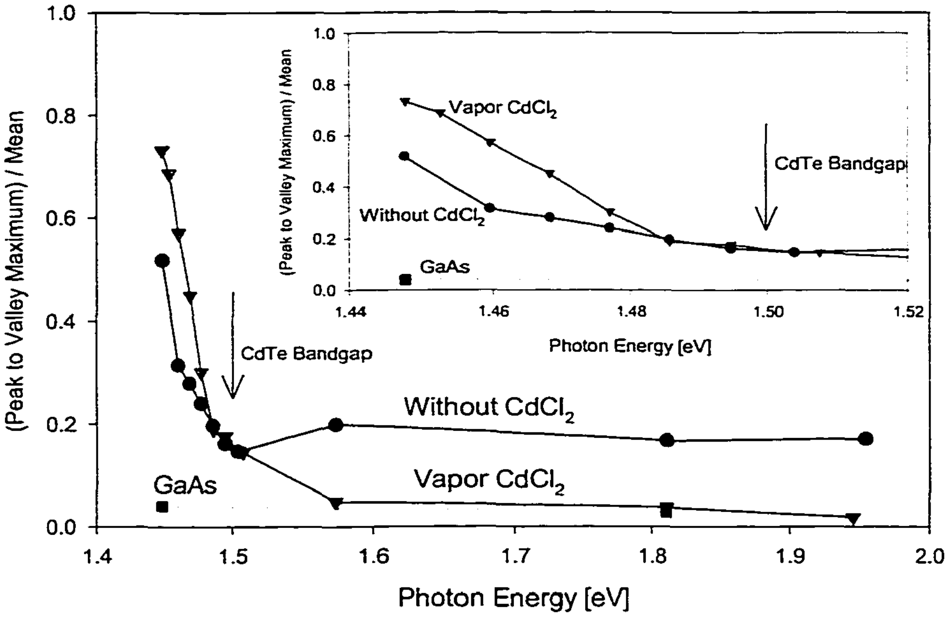

Figure 5.13. Variation in collected current over a 50×10 micron area for various photon energies.

In contrast to the discussion of bandgap variations in Section 5.4, however, the regions of reduced bandgap do not correlate with defects, as shown in Figure 5.14. This series of graphs show high resolution data over a 50×10 μm area (in contrast to the 500×100 μm area shown in Figure 5.9), indicating the size of the reduced bandgap regions is also much smaller in this case. This observation suggests that the lower bandgap material is not necessarily of poorer quality than surrounding regions.

Local bandgap variations may result from non-uniformities at the interface (such as an island of CdS or a void of CdTe). The increased surface area available to the CdCl$_2$ treatment may lead to increased alloying, as also discussed above. Another possibility is that the variations result from non-uniform penetration of CdCl$_2$ to the interface. It is clear,

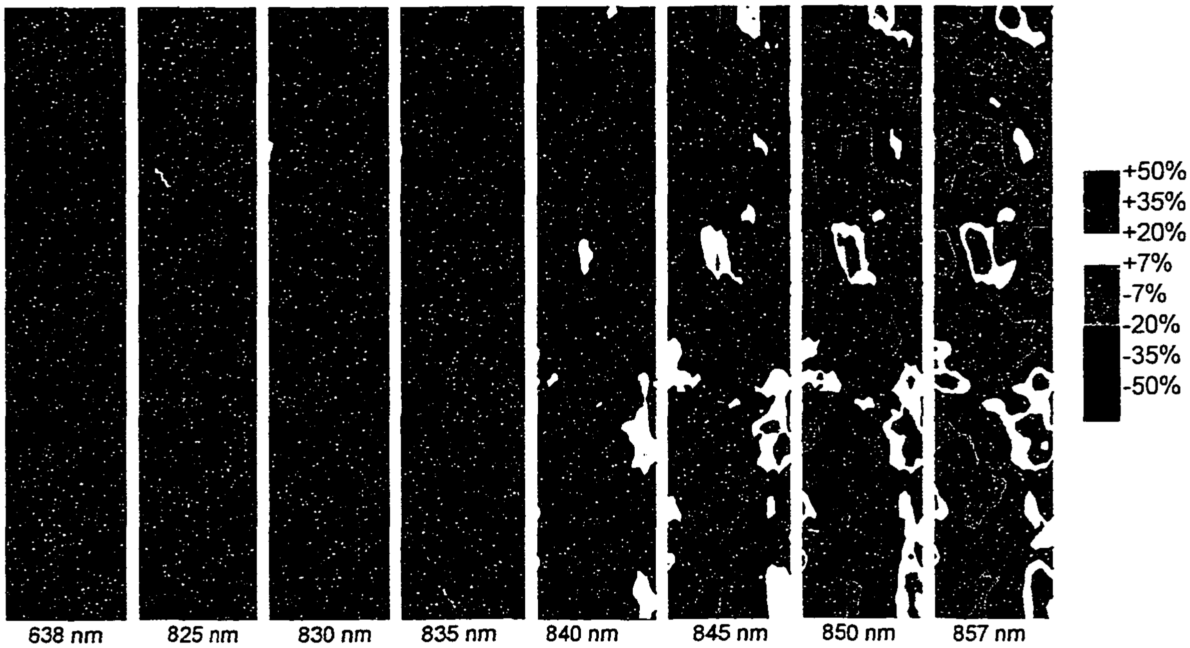

Figure 5.14. Response over a 50×10 micron area on the $CdCl_2$ treated cell with multiple wavelengths as labeled. The contrast in each case is consistent with the variation from the mean value. Identical conditions were used for each set of data: 1 micron spot, 1 sun illumination.

however, that local bandgap variations do not in all cases correlate with regions in increased resistivity, suggesting the alloyed layer is not necessarily responsible for the high resistance exhibited by local regions of the cell in Section 5.4.

5.6 Stress-induced Effects

The long-term (30 year) stability of CdTe solar cells has been of major interest to the manufacturing community. Accelerating testing with elevated temperatures has been investigated in some detail [39—41]. Typical changes includes loss of open-circuit voltage and fill-factor, with eventual losses in the short-circuit current at high temperatures and long stress times. Whether the losses are due to degradations of the cell as a whole, or due to degradations of local areas has to date not be examined.

Toward this end, data on the NREL CdTe cell examined in the previous section (with the $CdCl_2$ treatment) was taken before and after 10 days of stress, which involved placing the cell under ~2 suns of broad-spectrum light where it reached a temperature of 100 °C under open-circuit conditions. This set of conditions typically produces significant degradations in cell performance. The JV and QE curves before and after the stress are shown in Figure 5.15. The cell exhibited all of the above losses, but it did not show the "rollover" effect generally attributed to degradation of the back contact. The major component of the loss in short-circuit current is due to the falloff of the QE response in the 750 to 850 nm range, as seen in the lower graph of Figure 5.15.

The spatial variation in photocurrent response over the entire cell area before and after stress is shown in Figure 5.16. It is evident that the stress degrades certain regions more than others. The ability to find the same position on the sample before and after stress with high resolution allows the comparison of identical regions on the sample. Figure 5.17 shows medium resolution data taken on the regions within the squares in Figure 5.16. Note that the round feature which appears in the pre-stress case near the center of the graph is also found in the post-stress case. This serves to verify that identical regions are shown. The change in collection variation is again striking. Regions with reductions as high as 50% are found.

The use of the 857 nm laser over the same area as in Figure 5.17 indicates that the regions that degrade more with stress also show the reduction in bandgap attributed to sulfur alloying in the previous section. Figure 5.18 shows data taken after stress, and indicates that the degraded regions correlate strongly with the regions that show a reduced bandgap. Note that data taken before stress on a portion of the region shown indicates that the same

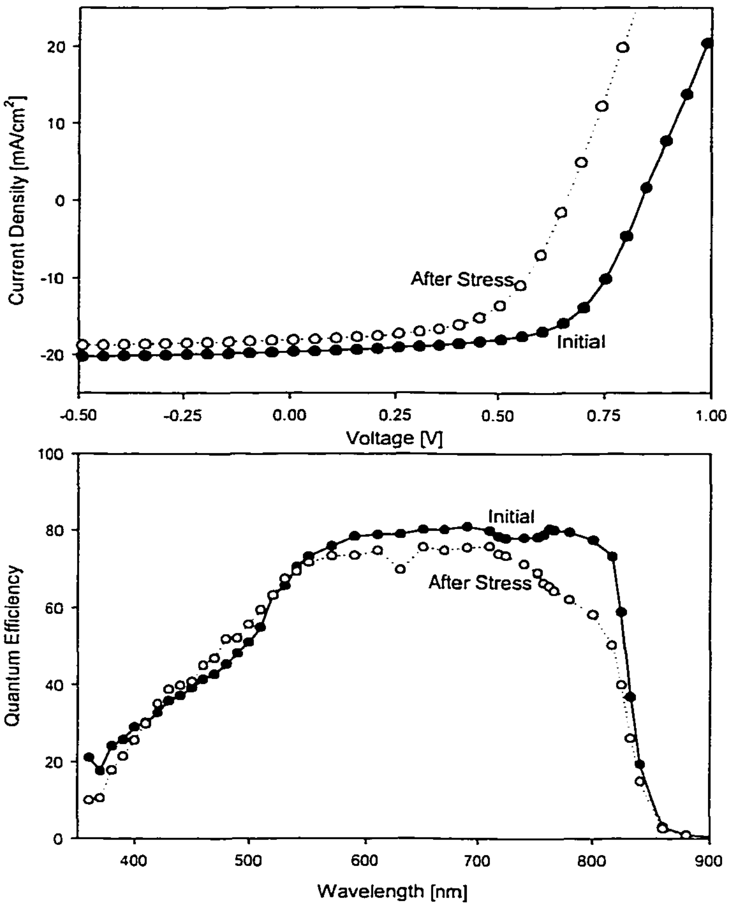

Figure 5.15. JV and QE curves of an NREL CdTe cell before and after 10 days of stress. The cell was illuminated under open-circuit conditions at 100 °C.

degree of bandgap variation was present before stress. Therefore, it appears that regions more susceptible to degradation induced by accelerated stress are also regions of reduced bandgap.

The bias dependence can again determine the types of defects which are induced locally by the stress. Figure 5.19 shows a portion of the post-stress data shown in Figure 5.17, with the points where AQE versus bias data was taken shown for reference. The graphs on the right show the bias dependent data for two intensities; a 10 μm spot was used in both cases. Fits to this data were again generated by modeling the equivalent circuit. The mod-

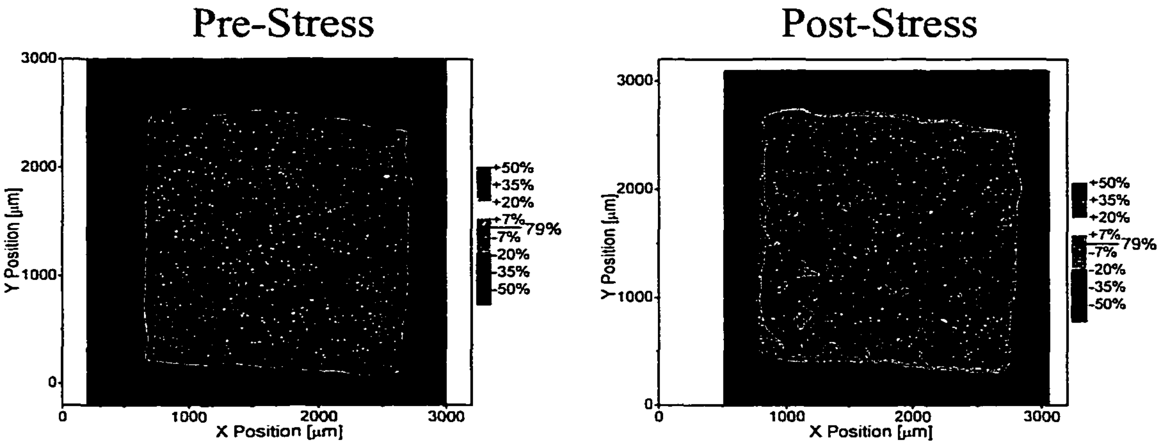

Figure 5.16. Variation in response before (left) and after (right) stress over the entire cell. Low resolution data.

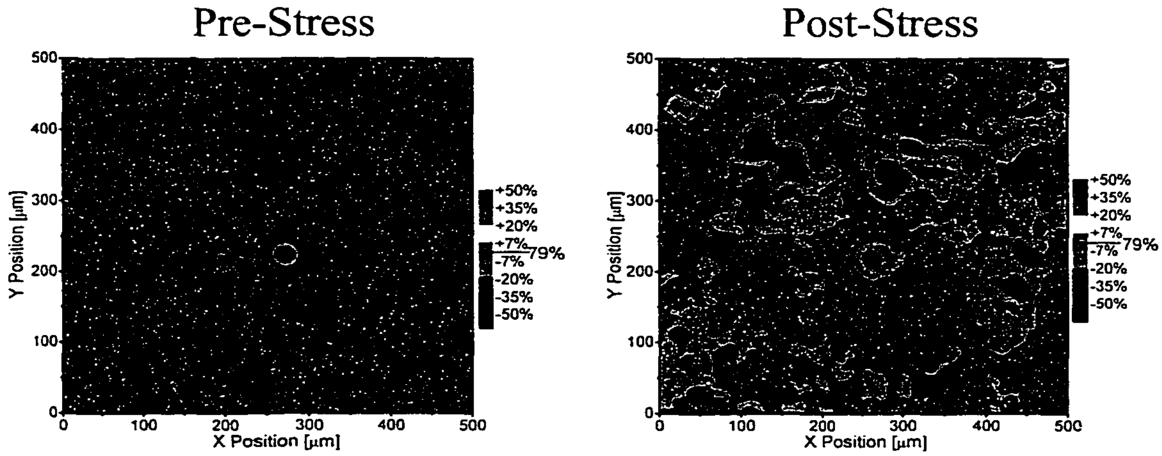

Figure 5.17. Variation in response before (left) and after (right) stress. Medium resolution data.

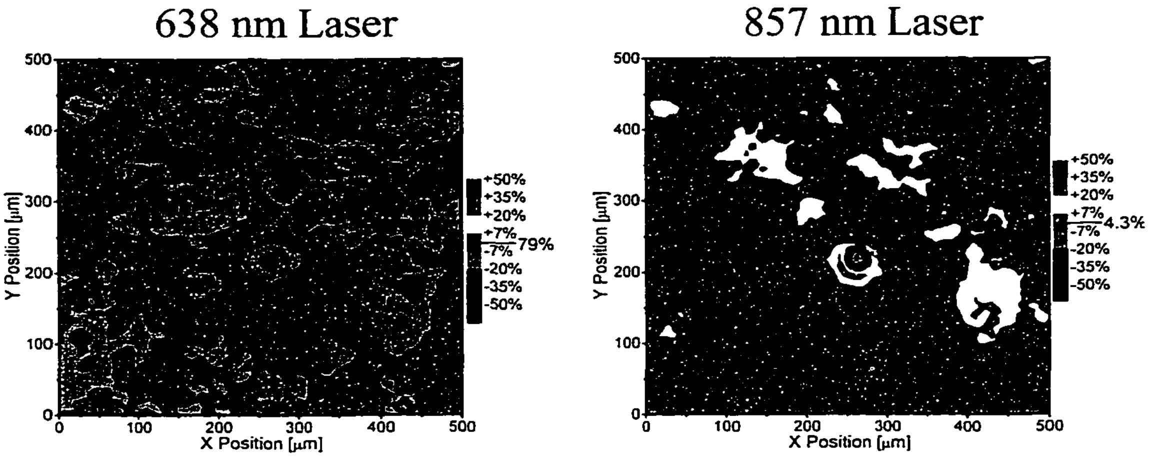

Figure 5.18. Comparison of post-stress variations with bandgap variations. Both graphs show post-stress data, however pre-stress data taken on a portion of the region indicates the bandgap variation was unchanged by stress. Medium resolution data.

eling indicates that the defects are primarily due to variations in the series resistance, with implied resistivities ranging from 0.4 $\Omega\,\mathrm{cm}^2$ to over 2 $\Omega\,\mathrm{cm}^2$. Note that the best fits to the high intensity data were attained by assuming high injection. A secondary effect is again the present of shunting, which reduces the overall collection.

It is not entirely clear that the alloying is directly responsible for the local degradation. For instance, the amount of degradation exhibited by cells stressed under identical conditions has been shown to depend strongly on the amount of Cu used in the back contact [42]. In fact, different processing steps involving the back contact have been shown to strongly impact the degree of degradation seen in CdTe devices. One possibility for the correlation is that defects in the CdTe film allowed non-uniform penetration of $CdCl_2$ to the interface, causing variations in the amount of alloying. These defects would then also allow large amounts of Cu or other elements from the back contact to diffuse to the interface at elevated temperatures.

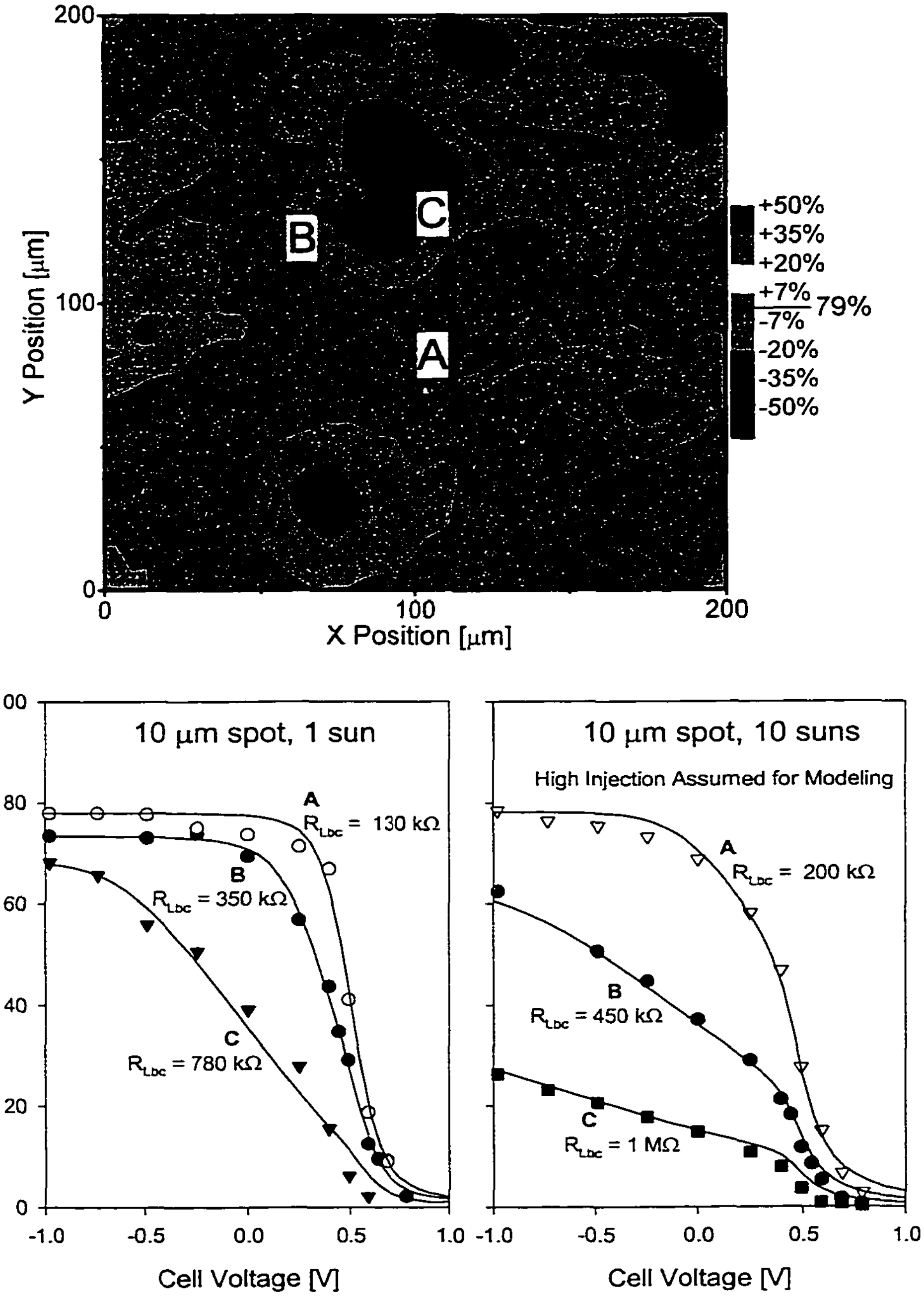

Figure 5.19. Data indicating regions where AQE versus bias data was taken, and the data at two laser intensities.

Chapter 6

Summary and Conclusions

This thesis has detailed the development of an apparatus capable of spatially mapping the photocurrent collection efficiency of solar cells. The apparatus is a complete computer-controlled instrument, which can take data at multiple resolutions, laser intensities, and wavelengths. The device under test can be held at an adjustable bias to permit evaluation of the causes of local reductions in collection. The ability to measure the photocurrent with micron resolution while 1 sun equivalent laser power is used is a key characteristic, since results directly correspond to the performance of the solar cell in field operation. The ability to find the same position on the sample with high resolution after it has been removed and replaced in the apparatus has allowed direct comparisons to be made of the effects of environmental stress on local regions on a device. Finally, interpretation of the data has been aided by modeling of an equivalent circuit, which allows separation of the causes of local reductions in the collection.

6.1 Apparatus

The optical system, which produces a near-diffraction-limited spot size, has incorporated single-mode fiber optics. The use of fiber allows multiple laser wavelengths to be used without realignment of components, while producing a nearly pure Gaussian spatial mode laser beam (necessary for producing the finely-focused laser spot). A beam splitter system allows the intensity at the sample to be monitored continuously, which allows direct evaluation of results in terms of the apparent quantum efficiency. This facilitates making comparisons between the response at different wavelengths and between various solar cell devices. The use of a microscope objective with an adjustable correction for focusing through glass has allowed high resolution data to be taken with glass-superstrate type devices, notably CdTe-based solar cells.

The cell mounting and positioning system allows the device to be positioned under the focused laser with 1 μm repeatability. If a mounted device is removed from the apparatus, the cell is typically replaced to within 50 μm of its initial position; any feature in the cell response allows one to relate the new position to the previous one, generally with 1 μm accuracy. The minimum step size of 0.2 μm is small enough to take advantage of the most finely-focused laser spot achieved.

Detection of AC signals in the range 10 μA to 0.1 nA has been accomplished with the used of a commercial transimpedance amplifier. This instrument allows the device to be biased, which again allows the causes of local reduction in collection to be separated. The measurements are typically performed by electronic intensity-modulation of the laser at 150 Hz, which allows phase sensitive detection to be used.

Control of the laser intensity, positioning stages, and electronics system is accomplished using LabView software. The software provides the user with real time display of experimental parameters. Data is typically written to text files for analysis with commercial software; additional LabView software has also been written for plotting both 1D and 2D data.

6.2 Modeling and Analysis

Interpretation of the bias dependent data acquired with this technique has been aided with Pspice simulation of an equivalent circuit. Curves generated with the simulation fit the data, allowing the separation of series resistance, shunting, and recombination effects. The application of this method to data taken on several solar cells has indicated that the most common cause of local reductions in the collection is local variations in the series resistivity of the material. Other effects considered are high injection, the dependence on spot size, variation in bandgap, and the temperature rise induced by the laser.

Analysis has showed that a first order effect of high injection is an effective increase in the diode quality factor. The resistance is expected to follow a straight-forward dependence on the spot size, since the current flow must be perpendicular to the junction. The wavelength dependence of collection near and slightly below the CdTe bandgap has been shown to be affected primarily by local variations in the bandgap, likely due to formation of the ternary compound $CdTe_{1-x}S_x$. This observation is supported by photoluminescence measurements performed on CdTe material by others. Finally, the calculated maximum temperature rise induced by the laser is the order of 1 °C, which is small enough to not perturb the device response significantly.

6.3 Results on Solar Cells

Several applications of this technique have been made on solar cells. Comparison of CdTe, CIGS, and crystalline GaAs cells indicate that all show relatively uniform collection over the active device area. The CdTe cells have been shown to contain the largest number of local electrical defects that reduce collection. These defects are primarily due to variations in the series resistivity of the material. In addition, these higher resistance regions often appear to be more strongly alloyed with sulfur, as measured by the degree of bandgap variation.

By comparing otherwise identical samples with and without a post-deposition $CdCl_2$ treatment, it has been shown that the $CdCl_2$ treatment improves the uniformity of collection for photons with energies above the CdTe bandgap. The treatment also, however, results in increased spatial variation in the material bandgap. In one case, however, the reduced bandgap regions did not initially show evidence of high resistance, suggesting that lower bandgap material is not a direct cause of high resistance.

Subjecting the cell to elevated temperature stress did, however, produce local increases in the resistivity of the material preferentially in regions where the decreased bandgap, i.e. increased sulfur alloying, was observed. The correlation between variations in bandgap and the increases in resistance may be due to non-uniform penetration of both $CdCl_2$ (which produces the alloying) and of contaminants from the back contact (which reduce the material quality).

These results suggest that the regions of reduced bandgap are not directly responsible for the high resistance defects. Instead, the cause of the cause of the bandgap lowering may also allow high resistance defects to be formed. This formation likely either takes place during the back contact anneal, as in the CSU cell, or during elevated temperature stress, as in the stressed NREL cell.

6.4 Conclusions

An instrument has been developed which is capable of generating the highest resolution maps of solar cell collection efficiency to date. The ability to generate data using 1 sun equivalent illumination at the highest resolution, with adjustable device bias, and with multiple laser wavelengths also makes the instrument unique. The application of the instrument to investigate variations in collection response of solar cells has yielded several insights on the effects of the $CdCl_2$ process and of environmental stress on local regions of devices. Direct evidence of spatial variations in the bandgap for CdTe solar cells, and their correlation with high resistance regions, has been presented for the first time. Finally, modeling of an equivalent circuit has been developed which allows separation of the causes of local reductions in the collection.

The observations in this thesis indicate that the path to deploying polycrystalline materials for terrestrial applications should include non-uniformity considerations. The instrument developed is expected to play a significant role in this effort by allowing the impact of uniformity to be systematically examined.

REFERENCES

[1] J. Bohland, I. Anisimov, and T. Dapkus, Proc. of the 26th PVSC , 355 (1997).

[2] J. R. Sites, J. E. Granata, and J. F. Hiltner, Solar Energy Materials and Solar Cells **55**, 424 (1998).

[3] X. Wu et al., Proc. of the 28th IEEE PVSC (2000).

[4] M. A. Contreras et al., Progress in Photovoltaics 7, 311 (1999).

[5] V. G. Karpov, R. Harju, and G. Dorer, Proc. of the 28th IEEE PVSC (2000).

[6] J. R. Sites and P. H. Mauk, Solar Cells **27**, 411 (1989).

[7] A. Fahrenbruch, NREL subcontract report (2000).

[8] D. Albin et al., Proc. of the 21st IEEE PVSC , 562 (1990).

[9] D. Albin et al., Proc. of the 21st IEEE PVSC , 562 (1990).

[10] D. Albin, personal communication, 2000.

[11] S. M. Sze, *Physics of Semiconductor Devices*, Wiley Interscience, 2nd edition, 1981.

[12] M. A. Green, *Solar Cells: Operating Principles, Technology and System Applications*, Prentice-Hall, New Jersey, 1982.

[13] A. L. Fahrenbruch and R. H. Bube, *Fundamentals of Solar Cells*, Academic Press, New York, 1983.

[14] S. J. Fonash, *Solar Cell Device Physics*, Academic Press, New York, 1981.

[15] A. E. Delahoy and A. M. Payne, Proc. of the 25th IEEE PVSC (1997).

[16] T. J. McMahon and B. V. Roedern, Proc. of the 26th IEEE PVSC , 377 (1997).

[17] S. A. Galloway, A. J. Holland, P. R. Wilshaw, A. W. Brinkman, and K. Durose, Proc. of the 13th Eur. PVSEC , 2072 (1995).

[18] S. A. Galloway, A. Brinkman, K. Durose, P. R. Wilshaw, and A. J. Holland, Appl. Phys. Lett. **68**, 3725 (1996).

[19] S. A. Galloway, P. R. Edwards, and K. Durose, Solar Energy Materials and Solar Cells **57**, 61 (1999).

[20] W. D. Sawyer, J. Appl. Phys. **59**, 2361 (1986).

[21] C. H. Seager, J. Appl. Phys. **52**, 3960 (1981).

[22] C. H. Seager, J. Appl. Phys. **53**, 5968 (1982).

[23] J. Marek, J. Appl. Phys. **55**, 318 (1984).

[24] J. D. Zook, Appl. Phys. Lett. **37**, 223 (1980).

[25] J. D. Zook, Appl. Phys. Lett. **42**, 602 (1983).

[26] W. VanRoosbroeck, J. Appl. Phys. **26**, 380 (1955).

[27] A. E. Dixon, S. Damaskinos, B. A. Oliver, and R. T. Adsett, J. Can. Ceramic Soc. **53** (1984).

[28] M. Rinio, H. J. Möller, and M. Werner, Sol. State Phenom. **63**, 115 (1998).

[29] J. R. Sites, H. Tavakolian, and R. A. Sasala, Solar Cells **29**, 39 (1990).

[30] P. Edwards, *Beam-Induced Current Studies of CdTe/CdS Solar Cells*, PhD thesis, University of Durham, 1998.

[31] X. Wu, P. Sheldon, T. Coutts, D. Rose, and H. Moutinho, Proc. of the 26th IEEE PVSC (1997).

[32] L. M. Woods, *Characterization of CdTe Grain-Boundaries in CdTe/CdS Solar Cells*, PhD thesis, Colorado State University, 2000.

[33] D. Levi et al., Proc. of the 26th IEEE PVSC , 351 (1997).

[34] D. Levi et al., Proc. of the 2nd World PVSEC , 1047 (1998).

[35] R. Dhere et al., Proc. of the 26th IEEE PVSC (1997).

[36] R. Hill and D. Richardson, Thin Solid Films **18**, 25 (1973).

[37] M. Lax, J. Appl. Phys. **48**, 3919 (1977).

[38] F. Kelemen, A. Neda, D. Niculescu, and E. Cruceanu, Phys. Stat. Sol. **21**, 557 (1967).

[39] J. Hiltner and J. Sites, Proc. of the 28th IEEE PVSC (2000).

[40] J. Hiltner and J. Sites, Proc. of the 16th European PVSEC (2000).

[41] S. S. Hegedus, B. E. McCandless, and R. W. Birkmire, Proc. of the 28th IEEE PVSC (2000).

[42] J. F. Hiltner and J. R. Sites, Proc. of the NCPV (1998).